

## Active tectonics around the Mediterranean

**A 3000-year record of surface-rupturing earthquakes at Günanan: variable fault-rupture lengths along the 1939 Erzincan earthquake-rupture segment of the North Anatolian Fault, Turkey**

Jeff G. Fraser<sup>1,\*</sup>, Aurelia Hubert-Ferrari<sup>1</sup>, Koen Verbeeck<sup>1</sup>, David Garcia-Moreno<sup>1</sup>, Ulas Avsar<sup>1</sup>, Nathalie Maricq<sup>2</sup>, Alexander Coudijzer<sup>3</sup>, Nele Vlamynck<sup>3</sup>, Kris Vanneste<sup>1</sup>

<sup>1</sup> Royal Observatory of Belgium, Seismology Section, Brussels, Belgium

<sup>2</sup> Université Libre de Bruxelles, Département des Sciences de la Terre et de L'Environnement, Brussels, Belgium

<sup>3</sup> Ghent University, Department of Geology and Soil Science, Ghent, Belgium

**Article history**

Received December 18, 2010; accepted February 20, 2012.

**Subject classification:**

Paleoseismology, North Anatolian Fault, Earthquake faults: properties and evolution, Plate boundaries, motion, and tectonics.

**ABSTRACT**

The North Anatolian Fault is a ca. 1200-km-long, right-lateral, strike-slip fault that forms the northern boundary of the Anatolian plate. A damaging sequence of earthquakes ruptured almost the entire fault in the twentieth century. This study adds to the growing number of paleoseismic investigations of the 350-km-long 1939 Erzincan earthquake-rupture segment, which is towards the eastern end of the North Anatolian Fault in Turkey. Using three paleoseismic trenches located along ca. 2 km of the principal fault strand, this study determines the timing of five earthquakes prior to the 1939 earthquake. The first three of these earthquakes are correlated to historical earthquakes in A.D. 1668, 1254 and 499, and two further events were identified as occurring from 881-673 B.C. and from 1406-1291 B.C. ( $2\sigma$  age ranges). By comparing the earthquake timing determined in this study to results from other paleoseismic investigations of the 1939 rupture segment, it becomes clear that this historical rupture segment does not always rupture in unison. This analysis indicates that the A.D. 499 earthquake was the last time the 1939 rupture segment ruptured in unison; partial ruptures of the 1939 rupture segment occur more frequently, and can also produce large magnitude earthquakes ( $M_W > 7$ ).

**1. Introduction**

The Anatolian plate is moving towards the west, principally due to the collision of the Arabian plate into Eurasia (Figure 1a) [e.g. Flerit et al. 2004, Sengor et al. 2005]. During the twentieth century, a sequence of large magnitude earthquakes ruptured most of the North Anatolian Fault (NAF), which caused catastrophe for the local populations and infrastructure [e.g. Barka 1996]. This sequence of large earthquakes began with the 1939 Erzincan earthquake, and proceeded to migrate in a cascading sequence, first to the west, and then to the east and west [Stein et al. 1997]. The most recent large surface-rupturing earthquakes (where 'sur-

face rupturing' refers to rupturing of the ground surface) in the sequence occurred near the eastern end of the Marmara Sea in 1999 [i.e. Barka et al. 2002, Gulen et al. 2002]. Stein et al. [1997] modeled the Coulomb failure stress changes that were caused by the earthquakes of the twentieth-century earthquake sequence on the NAF. They showed that earthquake-induced stress changes can raise the probability of fault ruptures at other sites, where subsequent earthquakes can occur [Stein et al. 1997]. The fault rupture can cause a stress drop on a slipped fault and an increase in the stress at nearby locations, hence bringing nearby faults closer to failure [Stein et al. 1997]. Where nearby faults have already accumulated near-critical stress levels, this can trigger an earthquake. This process suggests a mechanism for the cascading twentieth-century sequence of large earthquakes on the NAF. However, it does require that the levels of stress along the sections of the fault that ruptured in the twentieth-century sequence were all at near-critical levels. This raises the question of whether the NAF always ruptures in a cascading sequence like that observed in the twentieth century.

Turkey has a long historical record of earthquakes [e.g. Ambraseys 1970, Guidoboni et al. 1994, Ambraseys and Finkel 1995, Ambraseys and Jackson 1998, Nur and Cline 2000, Guidoboni and Comastri 2005, Sengor et al. 2005]. We have compiled a list of historical earthquakes from various sources that might have ruptured all or part of the 1939 Erzincan fault-rupture segment (Table 1). Historical earthquake records are typically temporally precise and accurate compared to the results of paleoseismic investigations, which have relatively low precision in time because of the uncertainties inherent in constraining paleoearthquake ages. However, historical earthquake records are typically spatially imprecise (i.e.

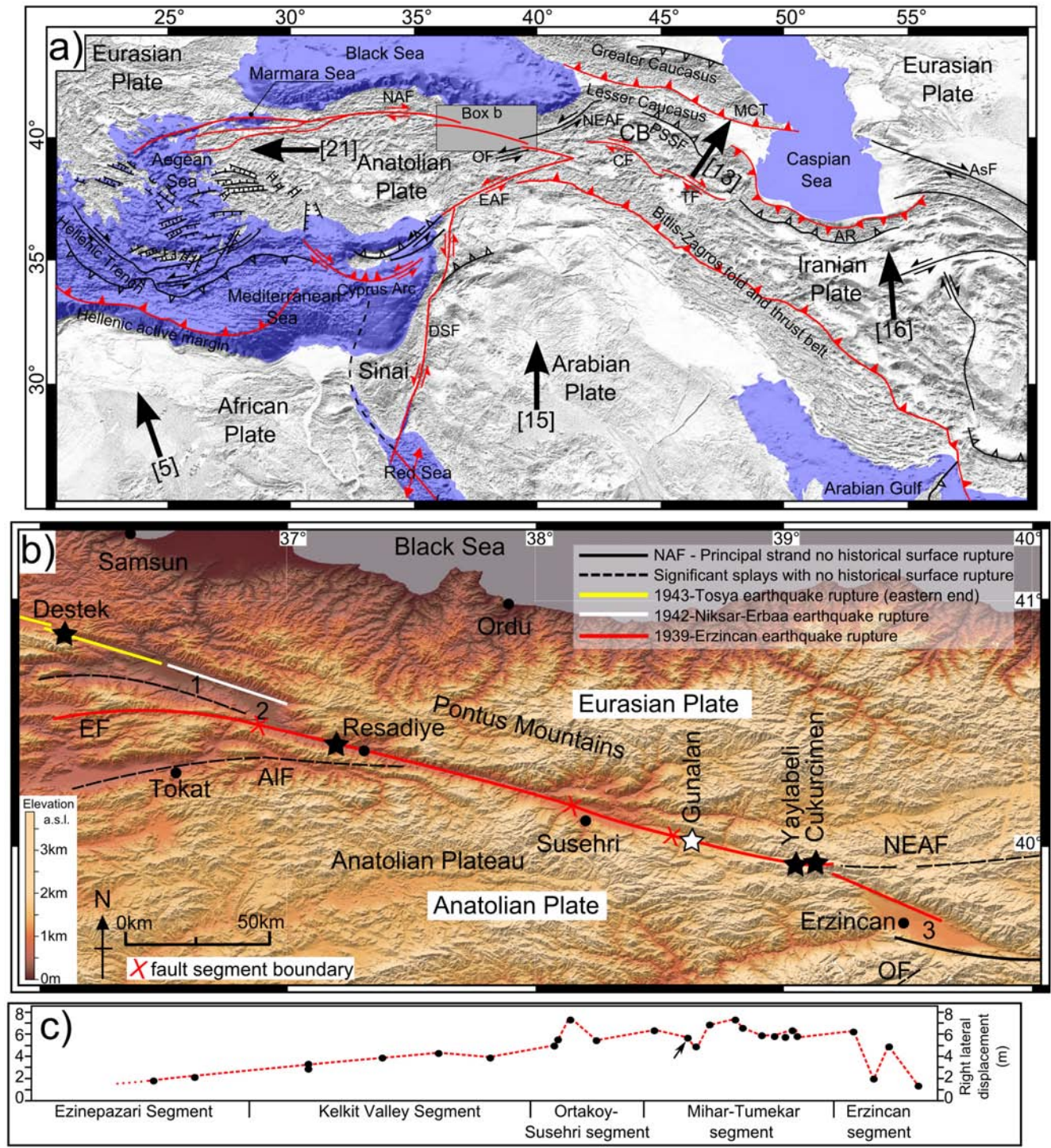


**Figure 1.** (a) Map of the Anatolian plate region. Heavy black arrows show the direction of plate motion based on GPS studies (relative to a fixed Eurasia), with the velocity in mm/yr shown in brackets [Reilinger et al. 2006]. Red lines depict present plate boundary faults, and black lines are important faults. DSF, Dead Sea Fault; NAF, North Anatolian Fault; EAF, East Anatolian Fault; NEAF, Northeast Anatolian Fault; MCT, main Caucasus thrust; AR, Alborz Range; CB, Caucasus Block; CF, Chalderan Fault; AsF, Ashgabat Fault; PSSF, Pembak-Sevan-Sunik Fault; and OF, Ovacik Fault. (modified from Fraser et al. [2010a]). (b) Map of 20th century earthquake ruptures near Güneş (location of map shown by rectangle labelled 'box b' in Figure 1a). Paleoseismic trench locations are shown with stars (this study white, other studies black), and filled circles show selected major settlements. Significant pull-apart basins are numbered: 1) Tasova–Erbaa pull-apart basin, 2) Niksar pull-apart basin and 3) Erzincan pull-apart basin. Significant fault splays are labeled: EF, Ezinepazari Fault; AIF, Almus Fault; and OF, Ovacik Fault. (c) Fault segments and right-lateral displacements associated with the 1939 Erzincan earthquake (modified from Barka [1996], see references therein). The irrigation canal offset by 5.6 m, ca. 2.5 km west of Güneş (Figure 2a) [Koçyiğit 1990, p. 165] is included in the Barka [1996] plot and indicated with an arrow.

it is seldom specified which fault or fault segment(s) ruptured to cause an earthquake), whereas paleoseismic investigations can yield earthquake records for a specific point on a particular fault strand. A paleoseismic trench investigation can con-

strain when a particular fault strand ruptured the ground surface. By using radiocarbon dating in conjunction with Bayesian statistical modeling [Biasi and Weldon 1994, Biasi et al. 2002, Hilley and Young 2008a, Hilley and Young 2008b],

we can obtain relatively precise paleoearthquake timing that incorporates the quantification of the uncertainty. By comparing the paleoearthquake timing with paleoseismic trench investigations at multiple sites along adjoining fault segments, we can estimate the ground-surface rupture length for large magnitude earthquakes (generally  $M > 6.5$ ), which is a proxy for paleoearthquake magnitude [e.g. Wells and Coppersmith 1994, Anderson et al. 1996]. The completeness of earthquake records from both historical and paleoseismic investigations is uncertain, because an absence of evidence is not evidence of absence (i.e. neither means of investigation provides a definitive complete record of surface-rupturing earthquakes). Therefore, combining the historical and paleoseismic data provides the best long-term spatiotemporal earthquake data.

To date, more than 50 paleoseismic investigations have been conducted along the NAF. In the present study, we focus on the 1939 Erzincan earthquake rupture segment. There have been many paleoseismic investigations along this segment, particularly in the area immediately west of the present study area; however, these results have not been published [i.e. conference abstracts: Okumura et al. 1994, Zabcı et al. 2008]. Investigations carried out at Resadiye [Fraser 2009b], Yaylabeli [Kozacı et al. 2011] and Cukurcimen [Hartleb et al. 2006] are publicly available.

This report presents a paleoseismic study at Günelan (40.024 °N; 38.627 °E), which is located on the 1939 Erzincan earthquake rupture segment (Figure 1b). The  $M_w$  7.7 Erzincan earthquake [Anderson et al. 1996] caused widespread damage and loss of life [Barka 1996]. The paleoseismic investigation at Günelan focuses on the construction of a long record of the timing of paleoearthquakes of the NAF. The paleoearthquake chronology determined in the present study was used by Fraser et al. [2010a], who summarized the publicly available paleoearthquake data relative to the NAF and compared the data from selected studies along the entire NAF. Günelan is located between previous paleoseismic investigations of the 1939 Erzincan earthquake rupture segment, at Resadiye [Fraser 2009b] to the west, and at Yaylabeli [Kozacı et al. 2011] and Cukurcimen [Hartleb et al. 2006] to the east (Figure 1b). In the present study, the timing of the paleoearthquakes determined at Günelan is compared with the timing of paleoearthquakes determined in the other paleoseismic investigations of the 1939 Erzincan earthquake fault-rupture segment and with the historical earthquake record (Table 1). The aim was to investigate the nature of the fault rupture along this section of the fault during the preceding seismic cycles.

## 2. Regional tectonic setting

Over geological time, as the Arabian plate moves northwards relative to the Eurasian plate, the wedge-shaped Anatolian plate is squeezed in an approximately north-south direction, which causes it to translate towards the west (Figure 1a). Back-arc extension in the Aegean region that is as-

sociated with subduction at the Hellenic arc might provide a pulling force on the Anatolian Plate [Flerit et al. 2004, Pondard et al. 2007]. The NAF formed in a similar tectonic regime as the present, and initiated in the east around 13 Ma [Sengor et al. 1985]. Using weaknesses in the lithosphere that are associated with pre-existing suture zones, the proto-NAF propagated westwards, and reached the Marmara Sea by about 5 Ma [Armijo et al. 1999, Hubert-Ferrari et al. 2002], although this is still debated [e.g. Sengor et al. 2005]. The offset features, such as suture zones, prominent geomorphic features, the Nıksar and Tasova–Erbaa pull-apart basins (Figure 1b), and other basins that developed during the formation of the NAF, suggest that it has undergone a total of approximately 85 km right-lateral offset [e.g. Barka et al. 2000, Sengor et al. 2005, Hubert-Ferrari et al. 2009].

The Holocene geomorphic offset features along the NAF suggest a slip rate of  $18.5 \pm 3.5$  mm/yr, with a right-lateral strike-slip style [Hubert-Ferrari et al. 2002]. A global-positioning system (GPS)-based study of the eastern Mediterranean region indicated that the rate of right-lateral, strike-slip deformation in the vicinity of the study area is approximately  $27.7 \pm 0.2$  mm/yr, with a negligible extensional component [Reilinger et al. 2006]. Thus, the Holocene slip rate is ca. 65% of the GPS-based slip rate. However, because the GPS data were only collected after the twentieth-century earthquake sequence, it might also include some post-seismic relaxation. Furthermore, because the GPS monitoring stations are mostly located at a significant distance from the NAF, the GPS rates also account for deformation on subordinate plate boundary structures (faults and folds) and intra-plate deformation. The comparison of the GPS-based and Holocene geomorphic-deformation-based slip rates suggests that most of the tectonic deformation associated with the northern edge of the Anatolian plate is accommodated by the NAF, with considerably less than 35% of the tectonic deformation accommodated as intra-plate.

The East Anatolian Fault accommodates the left-lateral, strike-slip deformation of the Anatolia–Arabian plate boundary, which is the south-eastern margin of the Anatolian plate. Other individual faults near the plate boundary and within the Anatolian plate are likely to be significantly less active (perhaps accommodating deformation of an order of magnitude less). For example, the Ovacik Fault and the Almus Fault (Figure 1b) accommodate some of the Anatolian–Eurasian plate boundary deformation within the Anatolian plate. Some of the Eurasian–Anatolian plate boundary movement is accommodated by faults to the north of the NAF; e.g. the Northeast Anatolian Fault (Figure 1b). Of note, the geological history and activity of many of these faults, and particularly of those located away from the principal plate boundary faults, are not well constrained. Therefore, it is only possible to speculate on the relationships concerning the crustal stress and strain between these faults and the NAF.

Year	Ref.	X	Comment
A.D. 1919	a	A	Reported ca. 50 km north of Resadiye.
A.D. 1754	b	B	Reported in Sivas.
A.D. 1684	b	A	Reported from Amasaya – refers to Niksar.
A.D. 1668	a,b,c	D	Reported widely in northern Turkey. Probably reflects more than one earthquake closely spaced in this year.
A.D. 1583	a	D	Extensive destruction in Erzincan.
A.D. 1579	b,c	B	Damage reported in Corum, Amasaya, and Erzincan Regions – may have been two separate events.
A.D. 1575	b	A	Reported November 5 in Erzincan. Probably a localized earthquake.
A.D. 1543	b	B/C	Reported April 4 in Corum, Tokat, and Erzincan.
A.D. 1535	b	A/B	Reported near Erzincan.
A.D. 1481/82	d	B	Extensive destruction in Erzincan.
A.D. 1457	d	B	Reported April 23. Extensive destruction in Erzincan.
A.D. 1374	d	B	Reported December 8. The Erzincan city walls collapsed.
A.D. 1287	d	B	Reported May 16. Extensive destruction in Erzincan.
A.D. 1254	a, d	E	Reported epicenter near Susehri, with damage also reported in Niksar and Erzincan.
A.D. 1236/37	d	A	Possibly doublet of 1206/7 A.D. earthquake. Caused collapse of a church in Erzincan.
A.D. 1206/7	d	A	Reported in Erzincan.
A.D. 1166	d	B	A strong earthquake reported in Erzincan. Possibly causing ca. 18000 deaths.
A.D. 1050	a, d	A	Reported at Cankiri (ca. 30 km south of Ilgaz).
A.D. 1045	a, d	B	Erzincan was destroyed along with many churches in the region.
A.D. 1043	e	A/B	A rupture from Nicopolis (ancient city near modern Susehri) in a line to Erzerum is reported.
A.D. 1011	a, d	A	Reported earthquake in Erzincan. There was also a major flood in this year – the damage may be compounded reflecting a smaller earthquake.
3rd, 5th, 7th centuries A.D.	e	?	Vague reports of seismicity in Amasya, Niksar, and Nicopolis. Exact dates are not available.
A.D. 499	a, d	E/D	Reported in Niksar and Nicopolis.
A.D. 343	f	A/B	Almost total destruction of Niksar. The localized location of reports suggest this event may have been similar to the 1942 Earthquake on the northern side of the Niksar basin.
c.1200 B.C.	g	D?	A sequence of earthquakes along the NAF may be attributable to the destruction of a collection of major cities at the transition of the Bronze Age to the Iron Age.

## References:

a: [Ambraseys and Jackson 1998]  
b: [Ambraseys and Finkel 1995]  
c: [Sengor et al. 2005]  
d: [Guidoboni and Comastri 2005]  
e: [Ambraseys 1970]  
f: [Guidoboni et al. 1994]  
g: [Nur and Cline 2000]

X – this column denotes our interpreted likelihood of rupture of the 1939 rupture segment of the NAF:

A: Probably did not rupture this segment  
B: Possibly ruptured part of the segment  
C: Possibly ruptured the whole segment  
D: Probably ruptured part of the segment  
E: Probably ruptured the whole segment

**Table 1.** Summary of historical earthquakes in the region of the 1939 Erzincan earthquake rupture segment.

### 3. Fault segmentation

Active fault traces are generally not continuous, as they have discontinuities that appear as steps or bends in the fault geometry. Depending on their scale, such discontinuities can slow or stop fault-rupture propagation [Wesnousky 2006].

On strike-slip faults, map-view steps in the fault trace can cause transpressional or transtensional stress, which results in forms such as pop-up structures and pull-apart basins, respectively. Wesnousky [2006] studied the importance of the size of discontinuities for fault-rupture propagation using his-

torical earthquakes on strike-slip faults, and found that discontinuities with step-over distances of up to 4 km can be ruptured across in an individual event, although smaller discontinuities can sometimes inhibit fault-rupture propagation.

'Fault-rupture segments' are sections of a fault that have ruptured during an earthquake. Thus, to define a fault-rupture segment, the extent of ground-surface rupture must be mapped either soon after an earthquake or by detailed observations of relict geological and/or geomorphological features caused by ancient surface ruptures (e.g. multiple paleoseismic studies along a fault).

'Fault segments' are sections of a fault that are bounded by discontinuities that can stop or slow fault-rupture propagation, and these are defined based on an assessment of the fault geometry.

The 1939 Erzincan earthquake fault-rupture segment of the NAF was described by Barka [1996], and references therein. It extended from the Erzincan pull-apart basin in the east, to near the village of Ezinepazari in the west (Figure 1b), with a rupture length of ca. 350 km [Anderson et al. 1996]. The western end of the rupture included the Ezinepazari Fault that splays to the southwest from the main NAF trace at the southern side of the Niksar pull-apart basin.

Barka [1996] partitioned the 1939 Erzincan fault-rupture segment into five fault segments, as illustrated in Figure 1b,c. He defined the segment boundaries by discontinuities in the map-view geometry of the active fault trace. The Ezinepazari and Kelkit Valley segments intersect at the south side of the Niksar pull-apart basin, the western and eastern ends of the Ortakoy–Susehri segment are defined by significant bends in the fault trace, and the Mihar–Tumekar to Erzincan fault-segment boundary is defined as a 20° restraining bend [see Barka 1996, for further details].

The present study area is located near the western end of the Mihar–Tumekar fault segment [Barka 1996] (Figure 1), on the southern side of the Golova Basin. Koçyiğit [1990] described the Golova Basin as an active basin along this segment of the NAF, and Koçyiğit [1989] described the Susehri Basin that is located immediately west of the Golova Basin as an active fault-wedge basin. We speculate that the Golova and Susehri Basins were originally one pull-apart basin that was superseded by a new optimally oriented principal deformation zone through the pull-apart basin. This superseding of the proto-Susehri–Golova pull-apart basin might have been coincident with the superseding of the Tasova–Erbaa pull-apart basin ca. 125 km to the west (Figure 1b), which was documented by Barka et al. [2000]; however, a detailed neotectonic study will be required to support this hypothesis. The presence of these neotectonic structures might have an influence on fault-rupture propagation of the Mihar–Tumekar and adjacent fault segments.

The present study presents the findings from a paleoseismic study on a section of the NAF at Günalan. We com-

pare the timing of paleoearthquakes identified at Günalan with those obtained from three other locations along the 1939 rupture segment, to determine whether the fault segments that ruptured in the 1939 Erzincan earthquake always rupture in tandem.

#### 4. Tectonogeomorphology of the study area

In the present study, we used tectonic geomorphology to identify the principal fault across which to undertake paleoseismic trenching studies, to investigate the timing of the paleoearthquakes. No tectonogeomorphic measurements were made in the present study. The study area is located on the southeast side of the Cobanlı River, near the village of Günalan (40.024 °N; 38.627 °E) (Figure 1b). There are three clearly active fault strands in the study area (Figure 2a), which we refer to as Faults A, B and C, from north to south (Figure 2).

In this area, Koçyiğit [1990] documented a broad (ca. 12-km fault-normal) damage zone that was caused by the 1939 earthquake, with small vertical displacements on many faults, although the majority of the slip (right-lateral) was accommodated by the principal deformation zone fault (equivalent to Fault A in the present study). The width of the damage zone might reflect reactivation of the structures associated with the Golova Basin to the north.

Koçyiğit [1990] measured four right-laterally offset features near the study area, on the principal deformation zone fault (Fault A), although we were not able to identify these features during our field work. The three right-lateral offsets were accompanied by 0.3 m to 3.5 m vertical displacement, and comprised: (1) a field boundary offset by 5.5 m, ca. 18 km west of Günalan; (2) a field boundary offset by 6.4 m, ca. 13 km west of Günalan; (3) a line of poplar trees offset by 5.7 m, ca. 5 km west of Günalan; and (4) an irrigation channel offset by 5.6 m, ca. 2.5 km west of Günalan (Figure 2a) [Koçyiğit 1990, p. 165]. The right-lateral offset (4) was used by Barka [1996] and is shown in Figure 1c. Additionally, Koçyiğit [1990, p. 165] noted three locations where, "... the southern and northern blocks alternately subsided and uplifted up to 3.5 m", and these were located: (5) ca. 300 m east of Günalan (Figure 2a); (6) ca. 600 m northeast of Günalan (Figure 2a); and (7) ca. 14 km east of Günalan. Koçyiğit [1990] described a splay of the principal deformation-zone fault that traces along the northern side of a prominent elongate linear ridge, as shown in the middle of Figure 2c, e, on which offset (6) was attributed to the 1939 earthquake. We recognized a lateral spread in this area (Figure 2c, f), but there was no evidence of faulting. Lateral spreads are a type of shallow translational landslide that can occur on gently sloping to flat ground, and they are relatively abundant during earthquakes due to failure on zones of liquefied soils [Keefer 1984]. Discussions with local residents indicated that this lateral spread occurred, or was at least reactivated, during the 1939 Erzincan earthquake. We therefore interpret that this offset as at-

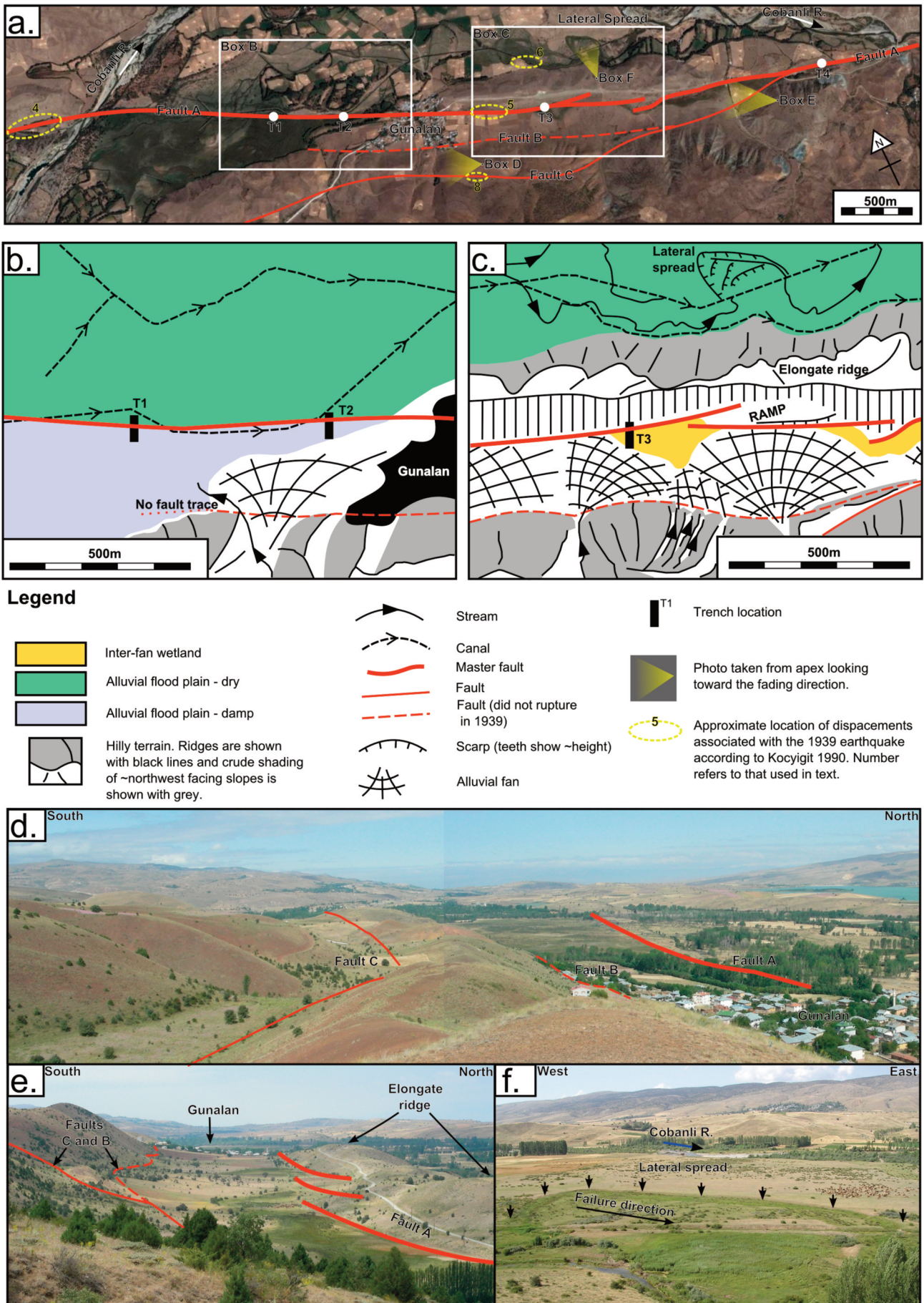


**Figure 2.** (a) Fault map of the study area over a satellite image with key features highlighted. (b, c) Geomorphologic maps of areas near paleoseismic trenches. (d) Photograph showing Faults C and A. (e) Photograph showing Faults A and B, and the depression in between. (f) Photograph showing the lateral spread the structure that is depicted in box c. The locations and orientations of the photographs in Figure 2 d-f are shown in Figure 2a.

tributable to the lateral spread. Koçyiğit [1990, p. 165] also noted that the southern strand (Fault C) of the bifurcated Cobanlı Fault (Faults B and C) were "reactivated by ground ruptures" during the 1939 earthquake (see Figure 2a, label 8). Based on the geomorphological expression of the three fault strands in the study area, we agree with the Koçyiğit [1990] interpretation of the relative activity of fault strands A, B and C. The very clear tectonogeomorphic features (described below) associated with fault A suggest that this was the principal deformation zone. Fault C has clear geomorphic expression, which suggests that this strand ruptured in the 1939 earthquake, while Fault B has a less clear geomorphic expression, which suggests that this strand did not rupture in the 1939 earthquake.

The features of the study area are described from west to east (Figure 2). The Cobanlı River flows towards the north, until it crosses the NAF, downstream of which it bends and flows towards the east (Figure 2a). The geomorphology of the western portion of the study area is an alluvial flood plain, across which Fault A is revealed by a subtle fault scarp (i.e. less than ca. 0.2 m high) that steps down to the south. The ground is considerably wetter on the south side of the fault, which corresponds to a recognizable change in the vegetation color (Figure 2b). Southeast of the alluvial plain, the terrain is hilly, and is dominated by linear ridges that run sub-parallel to the fault. We attribute these linear ridges to low-activity (relative to Fault A), possibly reactivated, fault strands. Local ephemeral streams, which generally flow towards the north, have eroded gullies through the linear ridges at some locations. The village of Günalan is situated near the point where the trace of Fault A leaves the alluvial plain to the west and passes into the hilly terrain (Figure 2a), where it runs along the southern side of the aforementioned elongate linear ridge, to approximately 3 km east of Günalan. Alluvial fan and wetland deposits fill a depression that has formed between the hills to the south and the elongate linear ridge (Figure 2c).

This elongate linear ridge is composed of Pliocene continental clastics of the Cobanlı Group that are part of the Upper Pontus Formation [Barka 1992]. There are three possible scenarios that would explain the formation of this feature (in order of preference):

(1) Strike-slip offset Pliocene deposits that make this primarily a shutter ridge. For this scenario, there is no need for a bounding fault on the northern side of the ridge, as river erosion alone can explain the concave slope break along the northern side of the elongate linear ridge. This is consistent with our interpretation that the fault mapped by Koçyiğit [1990] on the northern side of the elongate linear ridge is attributable to a lateral spread.

(2) A pop-up-structure or pressure ridge. For such a feature to form, there would also need to be a fault on the northern side of the elongate linear ridge, for which we did

not recognize any geomorphological evidence.

(3) A significant and consistent dip-slip component of displacement down on the south side of the fault might have caused the topographic step on the south side of the ridge. The topographic step down to the north on the northern side of the ridge might have been caused by river-bank erosion. Thus the elongate ridge would be the remains of an elevated area, the northern part of which was eroded away by the Cobanlı River.

While we cannot rule out any of these three scenarios, we believe that scenario (1) is the most probable, and it is the simplest explanation. Regardless of how the elongate ridge formed, it is clearly bounded by a fault on its southern side and the concave slope-break at its base traps small alluvial fans from local northward draining ephemeral streams. The fans have a typical conical geometry, with apices in small valleys that drain the hills to the south. Between the alluvial fans, where they abut the fault scarp, reed beds and associated organic-rich wetland deposits have developed.

South of the elongate linear ridge, Faults B and C splay southward. Our interpretation of the local geomorphology is that the depression between Faults A and B (which the alluvial fans are filling) reflects long-term incremental subsidence, and the linear ridge between Faults B and C reflects long-term incremental uplift. Sediments are trapped as a consequence of the linear ridge between Faults B and C, and these form a flat area on the south side of Fault C (Figure 2d).

To the east of the junction of Faults A and C, Fault A has a relatively simple straight trace across a terrace of the Cobanlı River. The ground surface to the north of the fault is slightly folded, forming a subtle anticline (the eastwards continuation of the linear ridge) that traps fine-grained sediments on the south side of the fault. The vegetation is darker on the south side of the fault. Near the eastern end of the field area (Figure 2a), field observations indicate that saline water ponds are forming a salina on the south side of the fault, and travertine is forming on the north side of the fault.

## 5. Paleoseismic trenching

To investigate the variability of the fault rupture lengths along the 1939 Erzincan earthquake fault rupture segment in comparison with the results of paleoseismic investigations, we require long records of earthquake timing that incorporate as many seismic cycles as possible. In the light of this objective, the present study used a paleoseismic trenching strategy to obtain the longest possible record of earthquake timing, rather than to focus on collecting other paleoseismic parameters, such as the offset per event and the slip rate. In particular, this involved constructing trenches perpendicular to the fault in locations with prolonged, distinctive, and relatively continuous or frequent sedimentation, which provides evidence of numerous paleoearthquakes and can be safely exposed in a paleoseismic trench. These trenching lo-

cation attributes were traded-off against locations where piercing points might be encountered that could yield the rates of horizontal and vertical deformation.

We selected a number of potential paleoseismic trenching locations in the study area, and we evaluated them by the opening of test pits. Apart from the test pits across Fault C, where we encountered homogenous strata, all of the other test pits were across Fault A, but many were abandoned because of shallow groundwater (0.1 m to 1.0 m below the ground surface). Four test pits were expanded into paleoseismic trenches, and these were indicated as T1 to T4, from west to east (Figure 2a). Trenches T1 and T2 were located on the alluvial plain between the Cobanlı River and Günalan (Figure 2b). Trench T3 was by far the largest trench, and it was situated at the base of the fault-bounded southern side of the elongate linear ridge, in the inter-fan, fine-grained deposits (Figure 2c). Trench T4 (Figure 2a) was about 2 m deep (to the top of the groundwater table) and revealed evidence of two to four paleoearthquakes, which offset stratified, thinly bedded (ca. 5 cm) organic and inorganic deposits. Unfortunately, Trench T4 had to be abandoned because of a voluminous discharge (estimated 5 l/s) of unidentified gasses that might have been detrimental to health. Therefore, trench T4 is not discussed further here.

Paleoseismic trenches were logged in the field using a 1 m × 1 m (or smaller) string grid on the trench walls, and using a co-ordinate system with the origin located below the northern base of the trench. The stratigraphic units were logged, described and given unit symbols. Photograph mosaics of the trenches were made using photographs taken during dispersed lighting conditions. The photographs were corrected for spherical divergence and crudely for the geometry of the trench walls, although this was an imperfect process and is the reason for some of the discrepancies between the trench logs and the photograph mosaics. Further discrepancies might also be due to small-scale erosion and the cleaning of the trench walls between the trench logging and the trench photography. We describe the results of each paleoseismic trench in the following sections.

Paleoseismic trenches T1 and T2 revealed clear evidence of one and three paleoearthquakes, respectively. The more conventional evidence of paleoearthquakes in paleoseismic trenches T1 and T2 are used to validate the less conventional evidence of six paleoearthquakes revealed in paleoseismic trench T3. As the number of paleoearthquakes is relatively few in paleoseismic trenches T1 and T2, the age of the event horizons are described along with the evidence of paleoearthquakes. As there were more paleoearthquakes revealed for paleoseismic trench T3 and as the timing of these earthquakes was validated by the findings from paleoseismic trenches T1 and T2, this paleoearthquake timing record is described in a separate section on the paleoearthquake timing.

### 5.1. Paleoseismic trench T1

Paleoseismic trench T1 was excavated down to the groundwater table on the alluvial plain of the Cobanlı River (Figure 2). The trench revealed a faulted sequence of interbedded clay (Cn), silty clay and clayey silt (Fn), sand (Sn) and organic soils (Psn), overlying river gravel (Gxn). Figure 3 shows the trench log, Figure 4 shows a photograph mosaic of part of the east wall of the trench, and Table A.A-1 of Annex A gives the stratigraphic unit descriptions.

The fault deformation was located between about 9.5 m and 14 m on both walls of the trench, and comprised both discrete fault planes and zones of shearing that displace strata correlated between the north and south sides of the fault zone (based on structure, texture and composition). Trench T1 revealed evidence of one surface-rupturing earthquake (named as T1E0), based on multiple fault terminations at or slightly below the base of the sand unit S4 (in the west wall) and the base of the sand unit S3 (in the east wall). These horizons are stratigraphically equivalent, as S3 corresponds to undifferentiated sand units S2 and S4. The fault terminations a few cm below this horizon were interpreted as the same event, as the tips of strike-slip fault strands do not always rupture to the ground surface. Based on this interpretation, the northernmost fault scarp that formed in the event remained near vertical, while unit S4 was deposited. Cross bedding in the sand unit S4 (above the event horizon) suggests that it is an aeolian deposit, with the sand possibly blown from the bed of the Cobanlı River, or possibly reflecting an abundance of sand produced by liquefaction. This would explain why the fault scarp or free-face remained intact while unit S4 was deposited, because if the sand deposits were from a fluvial source, the free-face would be expected to have been more eroded.

The apparent vertical displacement revealed in the trench walls reflects four key variables: (1) the vertical component of displacement associated with the regional displacement vector; (2) the horizontal component of displacement associated with the regional displacement vector coupled with the along-fault strand changes in stratigraphic unit thicknesses and elevation; (3) the complex and highly variable fault displacement that resulted from local fault geometry in both the section and map views; and (4) settlement or heave that resulted from long-term and/or co-seismic processes, such as compaction and liquefaction. To quantify these components of displacement, and hence to be able to comment on the regional displacement, a three-dimensional perspective was required (e.g. from three-dimensional trenching or from detailed geophysical surveys). Therefore, we make no attempt to measure the displacement associated with this event. However, we do note that in this trench, the deeper soil horizons were displaced down to the south by around 1 m.

Our interpretation here is that the one event recorded in this trench is the 1939 Erzincan earthquake. To confirm our interpretation, we radiocarbon-dated a single sample (sam-

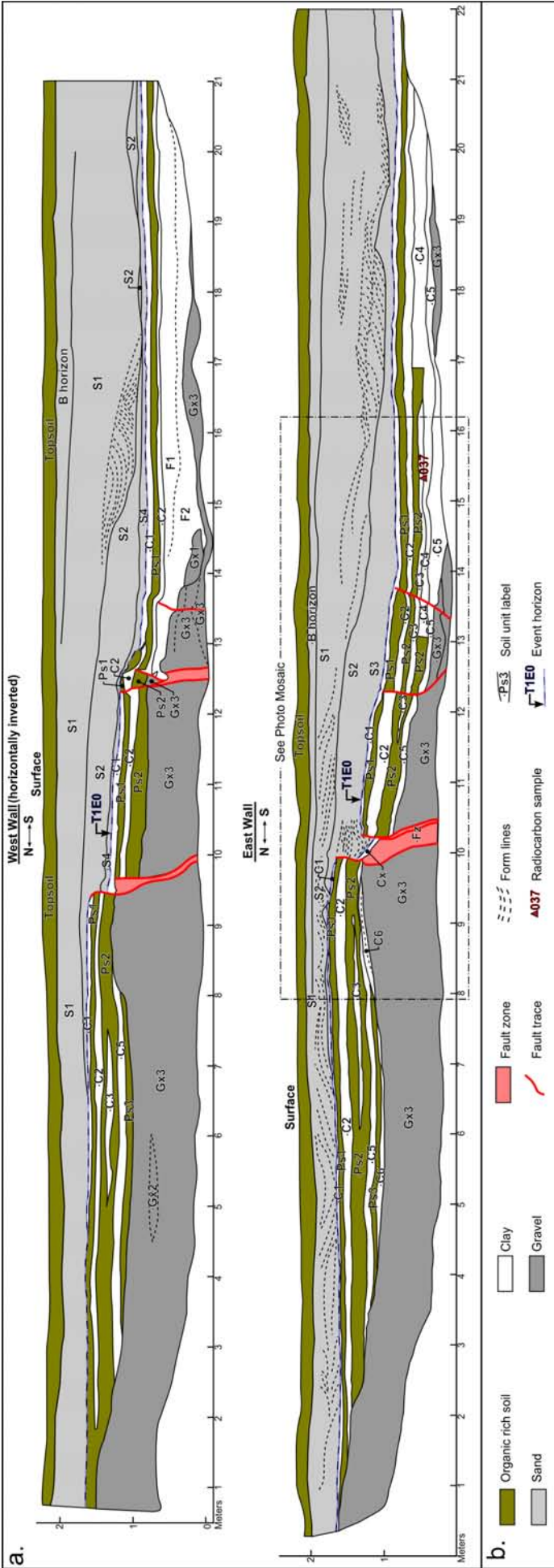
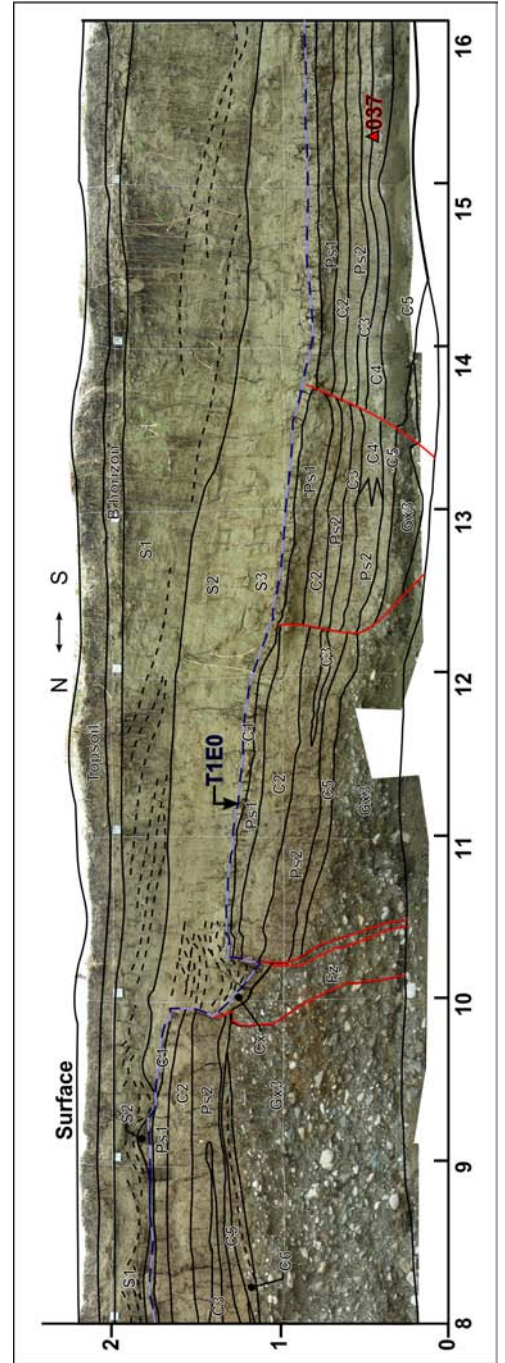


**Figure 3** (above). (a) Trench log of paleoseismic trench T1. The horizontal and vertical axes are labeled in meters. (b) Legend for box a. Unit symbols correlate to stratigraphic descriptions in Table A.A-1 (Annex A). See Figure 4 for a photograph mosaic of a section of the east wall.  
**Figure 4** (below). Photograph mosaic of a section of the east wall of paleoseismic trench T1. The horizontal and vertical axes are labeled in meters. Unit symbols correlate to stratigraphic descriptions in Table A.A-1 (Annex A). See Figure 3 for legend.



## FRASER ET AL.

Sample #	Soil unit	Trench wall	CRA (years B.P.)	Calibrated age years (A.D./B.C.) $2\sigma$	
				unmodeled	modeled
<b>Trench T1</b>					
T1E1: younger than A.D. 1494					
37	C4	E	270 $\pm$ 35	A.D. 1494 – A.D. 1951	not modeled
<b>Trench T2</b>					
T2E0 and T2E1: younger than ~1660 A.D.					
42	Ps1a	W	160 $\pm$ 35	A.D. 1663 – A.D. 1953	not modeled
41	Ps1a	W	170 $\pm$ 35	A.D. 1657 – A.D. 1953	not modeled
40	Ps1b	W	31700 $\pm$ 150	29995 B.C. – 29559 B.C.	reworked
47	Ps1b	E	1370 $\pm$ 40	A.D. 608 – A.D. 761	reworked
50	S9	E	340 $\pm$ 35	A.D. 1468 – A.D. 1641	not modeled
T2E2: A.D. 200 - A.D. 1640					
43	Ps2a	W	1750 $\pm$ 50	A.D. 137 – A.D. 402	not modeled
49	Ps2b	W	1720 $\pm$ 40	A.D. 242 – A.D. 399	not modeled
<b>Trench T3</b>					
26	W2	W	710 $\pm$ 40	A.D. 1227 – A.D. 1388	reworked
T3E0 - base of W2 - interpreted to be the 1939 earthquake					
2	F1	E	60 $\pm$ 35	A.D. 1693 – modern	A.D. 1706 – A.D. 1926
B51	Ps2	E	150 $\pm$ 40	A.D. 1666 – A.D. 1953	A.D. 1666 – A.D. 1888
B53	F2	E	600 $\pm$ 35	A.D. 1297 – A.D. 1411	reworked
T3E1 - base of W3					
27	F3b	W	550 $\pm$ 35	A.D. 1311 – A.D. 1434	A.D. 1337 – A.D. 1440
B54	W4c	E	530 $\pm$ 35	A.D. 1317 – A.D. 1440	A.D. 1324 – A.D. 1428
6	W4c	E	570 $\pm$ 35	A.D. 1304 – A.D. 1425	A.D. 1305 – A.D. 1413
T3E2 - base of W4					
B55	F3a	E	790 $\pm$ 35	A.D. 1190 – A.D. 1281	A.D. 1189 – A.D. 1280
5	F3a	E	730 $\pm$ 35	A.D. 1222 – A.D. 1296	A.D. 1224 – A.D. 1291
B57	F3a	E	990 $\pm$ 35	A.D. 989 – A.D. 1154	A.D. 989 – A.D. 1153
28	F3/4u	W	3120 $\pm$ 30	1490 B.C. – 1314 B.C.	reworked
B60	W5b	E	1410 $\pm$ 40	A.D. 576 – A.D. 667	A.D. 578 – A.D. 669
T3E3 - base of W5					
B61	F4a	E	1770 $\pm$ 40	A.D. 136 – A.D. 381	A.D. 133 – A.D. 379
B64	F4b	E	2360 $\pm$ 40	A.D. 536 – 380 B.C.	reworked
25	F4b	W	3830 $\pm$ 40	2458 B.C. – 150 B.C.	reworked
24	F4b	W	2140 $\pm$ 40	353 B.C. – 55 B.C.	338 B.C. – 52 B.C.
23	F5	W	2150 $\pm$ 50	359 B.C. – 54 B.C.	363 B.C. – 122 B.C.
B68	F5	E	2600 $\pm$ 30	815 B.C. – 672 B.C.	811 B.C. – 568 B.C.
33	W6	W	1900 $\pm$ 30	A.D. 27 – A.D. 213	too young
T3E4 - base of W6					
12	F6c	E	4260 $\pm$ 30	2919 B.C. – 2779 B.C.	reworked
16	F6c	W	1820 $\pm$ 40	A.D. 86 – A.D. 323	too young
B70	F6c	E	2640 $\pm$ 40	890 B.C. – 774 B.C.	897 B.C. – 789 B.C.
10	F6c	E	4190 $\pm$ 30	2889 B.C. – 2676 B.C.	reworked
B71	F6c	E	3030 $\pm$ 30	1394 B.C. – 1213 B.C.	1359 B.C. – 1134 B.C.
17	F6c	W	3020 $\pm$ 40	1390 B.C. – 1130 B.C.	1347 B.C. – 1127 B.C.
34	F6b	W	1670 $\pm$ 40	A.D. 258 – A.D. 429	too young
B72	S4	E	3060 $\pm$ 40	1417 B.C. – 1220 B.C.	1381 B.C. – 1266 B.C.

Sample #	Soil unit	Trench wall	CRA (years B.P.)	Calibrated age years (A.D./B.C.) $2\sigma$	
				unmodeled	modeled
T3E5 - base of W7					1406 B.C. – 1291 B.C.
B73	F7	E	3290 $\pm$ 30	1628 B.C. – 1500 B.C.	reworked
9	F8	E	1600 $\pm$ 40	A.D. 385 – A.D. 553	too young
B81	F9	E	3070 $\pm$ 30	1413 B.C. – 1268 B.C.	1420 B.C. – 1321 B.C.

**Table 2** (continues from previous page). Summary of sample radiocarbon ages from this study. CRA, conventional radiocarbon aAge [Stuiver and Polach 1977]. A table with more extensive data is presented in Table A.B-1 (Annex B). Figure 9 is a graphical presentation of the order-constrained Bayesian model (electronic supplement 1) compiled using selected samples from trench T3.

ple 37) from below the event horizon, which yielded a calibrated radiocarbon age of A.D. 1494 to present ( $2\sigma$  age range) (Table 2) (note that the term 'present' is used to reflect 1950, in agreement with Stuiver and Polach [1977]). Therefore, paleoseismic trench T1 provides evidence for one surface-rupturing earthquake that occurred on this segment of the fault from sometime between A.D. 1494 and the present.

### 5.2. Paleoseismic trench T2

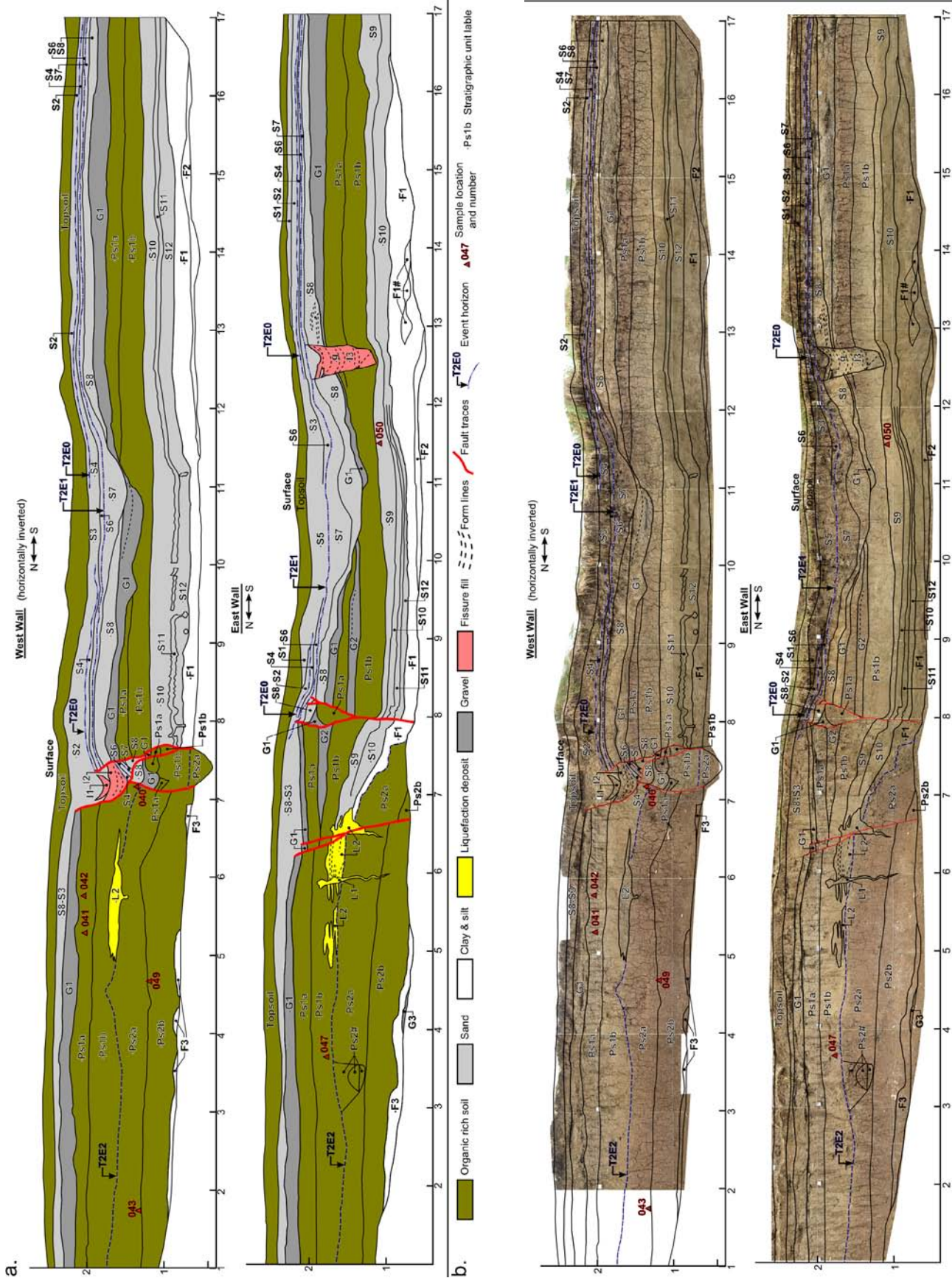
Paleoseismic trench T2 was excavated down to the groundwater table on the alluvial plain of the Cobanlı River, and it was closer to Günalan than trench T1 (Figure 2). The trench revealed a faulted sequence of organic rich soils ( $P_{sn}$ ), sand ( $S_n$ ), silt and clay ( $F_n$ ), and gravel ( $G_n$ ), with fissure infills ( $I_n$ ) and liquefaction deposits ( $L_n$ ). Figure 5 is a log of both of the trench walls, Figure 6 is a photograph mosaic overlain with the lines and labels of the trench log, and Table A.A-2 of Annex A gives the stratigraphic unit descriptions.

Distinct fault traces were recognized for both walls of the trench: between the horizontal distances of 6.5 m and 8.0 m on the west wall, and for a broader zone between the horizontal distances of 6.0 m and 8.5 m on the east wall (Figure 5). The faults displaced the stratigraphic units revealed in the walls of the trench, and they generally showed a down to the south displacement. Apparent monoclinical folding down to the north was revealed between the horizontal distances of 11 m and 12 m on the west wall, and between 11 m and 13 on the east wall (with associated tension cracking; see description below). Together, the faulting and folding revealed on the trench walls showed a graben bounded to the north by several faults and to the south by monoclinical folding; there was also a net displacement of around 0.5 m across the graben structure. As described above, these apparent vertical displacements reflect several mechanisms that we do not attempt to resolve in the present study.

Trench T2 showed evidence for three earthquakes, which we labeled from the most recent to the oldest as T2E0, T2E1 and T2E2. The evidence associated with the most-recent event, T2E0, is subtle, and therefore the evidence for T2E1 is described first. Event T2E1 was defined by fault terminations that extended to the base of the sand unit S6 on the east wall of the trench (i.e. Figure 5, at horizontal distances of 6.5 m and 8.0 m on the east wall). Coincident with

these fault terminations, there was a downward-tapering wedge-shaped deposit on the east wall, at the horizontal distance of 12 m to 13 m (Figure 5), which we interpreted as a fissure-fill deposit (Figure 5, I3). This fissure-fill deposit was interpreted to have formed in a tension crack that opened due to the folding of paleosols Ps1a and Ps1b down towards the fault, and to possibly be associated with some horizontal deformation. Evidence for the most-recent event, T2E0, was restricted to the fault zone on the west wall (at ca. 7 m on the horizontal axis), where there were two fissure-fill deposits (Figure 5, I1 and I2), which rested on a block of sand units (Figure 5, sand units S8-4) between two fault strands. The fault strand on the southern side of these deposits extended to the top of S4, which was a higher stratigraphic level than the faults on the east wall. Taken together, these observations suggested that the top of unit S4 is an event horizon, which we labeled as event T2E0, and that the base of the sand unit S6 is also an event horizon, which we labeled as event T2E1. Unfortunately, T2E0 is only revealed for the west wall, which considerably weakens the strength of our interpretation. Event T2E2 was revealed by a fault-zone unconformity that was accompanied by liquefaction. North of the fault zone on the west wall, the paleosol Ps2a was folded down towards the fault, whereas the overlying paleosols were flatter lying. Between the fault strands, at around a horizontal distance of 7 m on the east wall, the paleosol Ps2 was also folded down towards the southern fault, and it was overlain by fine-grained sediments and sand layers that thin to the north, which indicated an onlap onto a folded surface. The units between and including F1 and S9 that were exposed on the southern side of the northern-most fault strand on the east wall appear to have deposited onto a folded Ps2a (i.e. they thin to the north). Therefore, event horizon T2E2 can be constrained to between units Ps2a and F1. We interpreted the top of Ps2 to be a fault-zone angular unconformity. Therefore, we consider the top of the paleosol Ps2a to be the event horizon that corresponds to event T2E2.

Liquefaction deposits were recognized for both of the walls of the trench. It was assumed that the source layer(s) for the liquefaction deposits was below the strata exposed in this trench. L2 was a horizontally bedded sand deposit with pebble horizons that rested on top of Ps2a. L2 was only exposed for ca. 2 m on the trench wall, and became finer later-



From top: **Figure 5.** (a) Trench log of paleoseismic trench T2. The horizontal and vertical axes are labeled in meters. (b) Legend for box a. Unit symbols correlate to stratigraphic descriptions in Table A.A-2 (Annex A). **Figure 6.** Photograph mosaic of paleoseismic trench T2 overlain by the lines and unit labels of the trench log for comparison (Figure 5). The horizontal and vertical axes are labeled in meters. Unit symbols correlate to stratigraphic descriptions in Table A.A-2 (Annex A). See Figure 5 for legend.

ally, and eventually indiscernible from Ps1b. Near the center of the horizontal extent of L2, the deposit contained more pebbles and less bedding, and below its center it was connected to the upper part of a feeder dike that cross-cut Ps2a. We interpreted L2 as a surficial sand-blow deposit, which provided additional evidence that the top of Ps2a is an event horizon (T2E2). The liquefaction deposit L1 was a sub-vertical dike that terminated upwards in Ps1b and cross-cut L2, which was also faulted (at a horizontal distance of 6.5 m on the east wall). There was no evidence that this dike reached the ground surface, so it cannot be tied to a particular event horizon; however, it clearly occurred subsequent to T2E2 because of the cross-cutting relations. We attribute the liquefaction deposit L1 and the faults that offset the liquefaction deposit L2 to either of the more recent events of T2E0 or T2E1.

To constrain the age of the three event horizons in trench T2, seven samples were radiocarbon dated; details of the radiocarbon data and the units from which they were sampled are presented in Table 2. Samples 40 and 47 were clearly reworked as they were substantially older than the other sample ages, which suggested that the paleosol Ps1b comprised a significant component of reworked soils. Samples 41 and 42 (both from the paleosol PS1a) were the highest in the strata and provided the maximum age of both events T2E0 and T2E1. Both of the samples 41 and 42 had similar  $2\sigma$  calibrated age ranges of ca. A.D. 1660 to the present, which indicated that the two most recent earthquakes (T2E0 and T2E1) occurred sometime from A.D. ca. 1660 to the present (i.e. to 1950). The minimum age of event T2E2 was constrained by sample 50, and the maximum age by samples 43 and 49, which were very similar. Therefore, event T2E2 occurred sometime between A.D. 200 and A.D. 1640.

### 5.3. Paleoseismic trench T3

Unlike paleoseismic trenches T1 and T2, paleoseismic trench T3 was excavated to about 5 m depth and did not encounter groundwater. The trench revealed an interfingering sequence of stratigraphic units that comprised: gravel (Gn, Rg, Rgn, UG, or Ga), gravel wedges (Gnx), sand layers (Sn), organic rich soils (Psn), and fine-grained deposits (i.e. various mixtures of silt and clay) (Fnx). We interpreted that these stratigraphic units were deposited in a similar environment to that of the site today, which is a small inter-alluvial-fan wetland at the base of a fault scarp. During the period of deposition, the trench location might have evolved subtly; in particular, the wetness of the site due to climate, and/or tectonic and anthropogenic influences on drainage paths. Trench 3 was oriented perpendicular to the strike of Fault A (Figure 2), at the base of a steep (ca. 30°) south-facing slope (the southern side of the elongate linear ridge) composed of Pliocene clastic deposits [Koçyiğit 1990], which we described as poorly sorted gravel with silt to boulder-sized clasts. The strategy for trenching at this location was to be able to find

evidence for multiple fault ruptures (reflecting paleoearthquakes) in an area with regular and relatively continuous sedimentation. This location also had the advantage that different sediments were present on either side of the fault, as gravels to the north and inter-alluvial-fan wetland sediments (organics and distal fan deposits) to the south side of the fault; this can assist with the interpretation of the origins of the strata in the fault zone.

Figure 7 is a log of trench T3, Figure 8 is a photograph mosaic overlain by the lines and annotations from the trench log, and Table A.A-3 of Annex A provides the stratigraphic unit descriptions. The trench walls were benched with upper and lower walls that were separated by a ca. 1-m-wide bench (Figure 7). The distance between the bases of the lower walls was ca. 3 m.

#### 5.3.1. Fine-grained deposits

Fine-grained deposits were composed of silt and clay and were interpreted as distal alluvial fan deposits. We interpreted that these deposits were laid down relatively slowly by deposition of the suspended load of flood waters sourced from the low hills to the south of the trench site. This interpretation is consistent with the northwards tapering geometry of these units, where they interfingered with gravel wedges. The fine-grained soils might have included organic rich layers, although the decomposition of the organic content of these soils has rendered them indistinguishable from the fine-grained deposits below approximately 1 m below the ground surface. Organic rich soils in the top 1 m of the trench were interpreted as soils formed at the present ground surface (i.e. 'Topsoil'; Figure 7) or at former, now buried, ground surfaces (i.e. Paleosols 'Ps1' and 'Ps2'; Figure 7).

#### 5.3.2. Sand deposits

Distinctly continuous and recognizable (in the field) thin beds and laminae of sand (1 mm to 300 mm thick) were logged for both of the walls of the trench, and they provided very useful marker horizons in the strata. The sand layers were interbedded with the fine-grained and organic-rich strata to the south of the trench, and they were also interfingered with gravel wedges towards the northern end of the trench. Five sand layers were recognized for the west wall of the trench (S1-S5), which correlated to sand layers on the east wall, with the exceptions of the absence of sand layer S3 and the additional deeper sand layer S6 for the east wall. The origins of these sand layers remain uncertain. They might have been deposited by flood waters from the alluvial fans, or by aeolian processes, or perhaps they were associated with liquefaction on the less distal parts of the alluvial fan. It is unlikely that all of the sand layers were caused by liquefaction, because most of the sand layers do not correspond to the other evidence for paleoearthquakes that we present below.

The sand layers illustrate a clear increase in the dip,



down to the south, with depth. Regardless of the process of deposition that formed the sand layers, if they had been deposited on a slope with the angle near the base of the trench, we would expect to have seen an increased thickness away from the fault. Therefore, this dip must have formed after burial, as a consequence of tectonic deformation. The sand units were steeper near the fault, although south of a horizontal distance of ca. 10 m, the sand layers S1 and S2 were horizontal, whereas S4, S5 and S6 dipped at 4° to 7°. Unfortunately, there were no horizons where the angle between S2 and S4 can be justifiably measured, and therefore we cannot use the change in dip to identify event horizons. Nonetheless, the increasing dip of bedding with depth indicated that significant syndepositional tectonic deformation had occurred while this sedimentary sequence was being deposited. It also indicated that there was a down to the south displacement of the fault, and this indicated that the genesis of the elongate ridge described earlier did include some recognizable components of dip-slip displacement over time.

### 5.3.3. Gravel deposits

Numerous gravel units were labeled in this trench, in agreement with their properties and the interpretation of their origin. Stratigraphic descriptions are provided in Table A.A-3 of Annex A. The gravel units were partitioned into five groups, as follows:

#### 5.3.3.1. River gravels (Rg and Rgn)

The river gravels were interpreted to be much older than the other gravel units exposed in the trench, due to their intense deformation. We correlated this unit to the Pliocene continental clastics (Cobanlı Group) which formed the ridge to the north of the trench [Koçyiğit 1990, p. 157]. This unit might be equivalent to the structureless gravel (Ga).

#### 5.3.3.2. Undifferentiated gravels (UG)

This symbol is used for areas where no structure was recognizable due to bioturbation, although the material was interpreted as equivalent to the 'distinctive gravel units (Gn)' and perhaps to the 'gravel wedges (Wn and Wnx)'.

#### 5.3.3.3. Distinctive gravel units (Gn)

Particular distinctive colluvial gravel deposits were sourced from the slope to the north of the fault. Many of these units were probably equivalent to the 'gravel wedges (Wn and Wnx)', although due to the extensive faulting, which probably included significant (but unquantified) lateral displacement, and the lateral variability in the unit thickness and composition, these were seldom correlated across the fault. Many of the units represented undifferentiated combinations of differentiated units (e.g. unit G2 was the undifferentiated units G1 and G3). Gravel unit G13 was interpreted as a fissure-infill, based on its structure.

#### 5.3.3.4. Structureless gravel (Ga)

This gravel had no coherent internal structure. It is possible that this unit was a very large 'gravel wedge (Wn and Wnx)' unit; however, it is more likely that this was equivalent to the 'River gravels (Rg and Rgn)'.

#### 5.3.3.5. Gravel wedges (Wn and Wnx)

Gravel wedges are wedge-shaped stratigraphic units that interfingered with the fine-grained, organic-rich and sand deposits to the south. These wedges were composed of a range of materials, although they were mostly reworked 'river gravels (Rg and Rgn)', and they were interpreted as colluvial wedges. Each gravel wedge was given a number (n) when it was correlated to an equivalent unit on the opposite wall. Where the materials were different, a further sub-number (x) was used to provide separate stratigraphic unit descriptions.

### 5.3.4. Tectonostratigraphy

Two tectonostratigraphic features were used to identify the locations of event horizons: fault terminations and colluvial wedges. Most of the fault strands in the trench were located in the gravel units and were revealed by aligned clasts. Due to the difficulty of distinguishing the extent of the faults in gravel deposits (along with evidence of bioturbation near the ground surface), we have a low level of confidence for the stratigraphic location of fault terminations in this trench. We only logged the locations of faults where we were confident of their presence. In response to this low level of confidence, fault terminations were only used as supporting evidence for event horizons, and we relied more heavily on colluvial wedges.

A colluvial wedge is a deposit formed on the downthrown side of a fault by the collapse of a fault scarp (free face) during, or soon after (i.e. years to tens of years), an earthquake. The base of a colluvial wedge can be interpreted as an earthquake event horizon. We interpreted many of the 'gravel wedges (Wn and Wnx)' as colluvial wedges that were linked to surface-rupturing earthquakes. Arguably, these colluvial wedges might have been formed by localized failures of the steep slope to the north of the trench that were caused by nonseismic processes, such as extreme rainfall events. As the south-facing steep slope comprised a loose gravel deposit that had very little cohesion and negligible tensile strength, the localized slope failures were likely to be small (i.e. <2 m<sup>3</sup>), and therefore their associated deposits at the base of the slope would not be laterally continuous. Colluvial wedges caused by surface-rupturing earthquakes are expected to be more laterally continuous.

Colluvial wedges can be formed by two processes that are related to fault rupture, fault scarp retrogression (scarp collapse and subsequent erosion upslope, i.e. the 'classical' colluvial wedges that are direct paleoseismic evidence for a surface-rupturing earthquake), and widespread slope failures

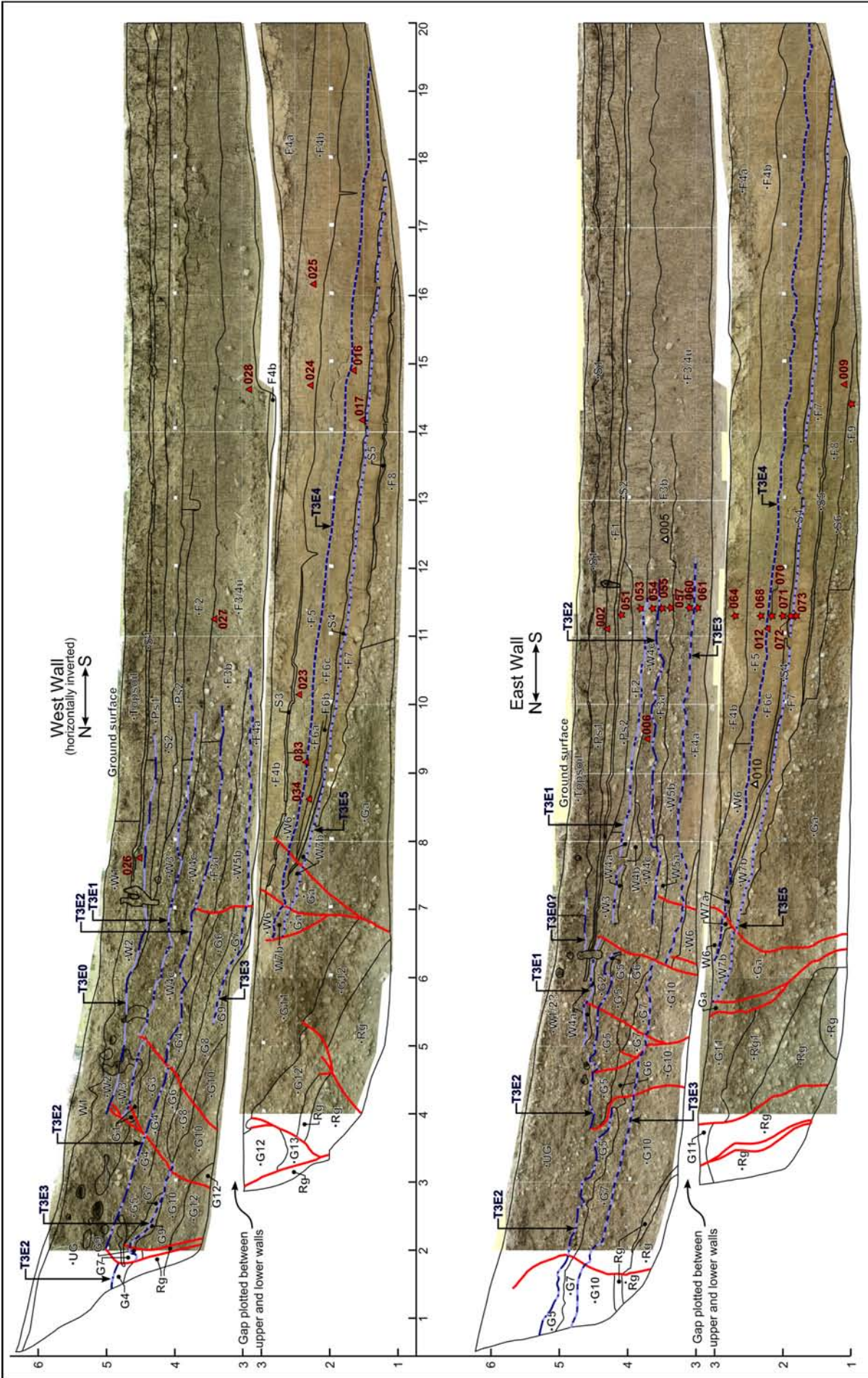


Figure 8. Photograph mosaic of paleoseismic trench T3 overlain by the lines and unit labels of the trench log for comparison (Figure 7). The horizontal and vertical axes are labeled in meters. Unit symbols correlate to stratigraphic descriptions in Table A.A-3 (Annex A). Note that a gap has been plotted between the upper and lower walls so that the whole logs can be seen. See Figure 7 for legend.

caused by seismic shaking (ground acceleration). All of these processes can mobilize a significant volume of gravel from the steep slope. We suspected that widespread slope failure as a consequence of high ground accelerations was the cause of the gravel wedges, because the amount of vertical displacement in the fault zone appeared to be limited (although this is not quantifiable in a single trench across a strike-slip fault). We used a similar approach to identify paleoearthquakes at two other locations on the NAF [Fraser et al. 2009a, 2010b]. To distinguish the localized slope-failure deposits from colluvial wedges, we considered opening two trenches on this section of the scarp, so that the lateral continuity of the gravel wedges could be assessed. However, groundwater was encountered at less than 1 m in depth in the nearby test pits, so instead trench T3 was constructed as wide as practical, with the upper walls ca. 5 m apart, and the lower walls ca. 3 m apart. South of the fault zone above the gravel Ga, we recognized seven distinct gravel wedges, all of which were present on both walls of the trench. We interpreted that gravel wedge W1 was related to the construction of a road along the slope immediately north of the trench (Figure 2e). The remaining six gravel wedges were interpreted as seismogenic colluvial wedges.

The amount of horizontal offset cannot be constrained in this trench. The amount of vertical offset was not discussed, as it cannot be used as evidence for displacement rates because of the unknown horizontal displacement and the potential range of orientations of any particular stratum.

The evidence for six paleoearthquake events, which we labeled as T3E0 to T3E5 from the most recent to the oldest are described below. The event horizons are shown and labeled in Figures 6 and 7, and Table A.A-3 of Annex A provides the stratigraphic unit descriptions.

#### 5.3.4.1. *Paleoearthquake T3E0*

The evidence for this event was a small colluvial wedge (gravel wedge W2) that was much more clearly evident on the west wall than the east wall, where gravel wedges W1 and W2 were not differentiated. Supporting evidence was provided by two fault terminations at the base of the gravel wedge W2 at a horizontal distance of ca. 4 m on the west wall. The supporting evidence for an event horizon at this stratigraphic position was an offset of the base of the preceding event horizons (T3E1 and T3E2) at a horizontal distance of approximately 5 m on the west wall.

#### 5.3.4.2. *Paleoearthquake T3E1*

This event corresponded to the base of the colluvial wedge W3. A fault termination at the base of colluvial wedge W3 at a horizontal distance of approximately 4.5 m on the west wall provided supporting evidence for this event horizon. On the east wall of the trench, there was a lack of distinctive strata immediately south of the fault zone, which

made the interpretation difficult. As gravel wedge W3 lay between sand S2 and gravel wedge W4a to the south of the fault zone, the event horizon was projected into the fault zone on the east wall along the top of the distinctive unit W4a. This showed an additional fault termination at a horizontal distance of ca. 5.75 m on the east wall.

#### 5.3.4.3. *Paleoearthquake T3E2*

The gravel wedge W4 was composed of three distinct units (W4a, W4b and W4c), and collectively, this wedge was larger than the more recent wedges. On the west wall of the trench, this event horizon was supported by fault terminations at a horizontal distance of 7 m, and if our interpretation that the gravel unit G3 corresponded to the gravel wedge W4c is correct, there was a fault termination at a horizontal distance of ca. 2 m below which the fault offsets the event horizon corresponding to an upslope-facing free face. As the gravel unit G2 was undifferentiated gravel units G1 and G3, a fault termination at its base at the horizontal distance of ca. 4.75 m on the east wall might also be considered as supporting evidence for this event horizon. The termination at a horizontal distance of ca. 4.75 m might pass through the event horizon by several cm, and this might reflect a small amount of slip associated with a subsequent event, or a lack of evidence for faulting due to bioturbation above the event horizon, or postseismic slip.

#### 5.3.4.4. *Paleoearthquake T3E3*

The gravel wedge W5 was interpreted to have formed as a result of this event, and its base was interpreted as the event horizon T3E3. Gravel wedge W5 was composed of two distinguishable units on the east wall (W5a and W5b), while only the lower unit (W5b) was present for the west wall. The event horizon was also defined as the contact between gravel units G7 and G9 further upslope. At some locations, these were indistinguishable and were collectively labeled as G8. For example, G8 was present between the horizontal distances of ca. 3.25 m and ca. 5.25 m for the west wall of the trench, and in this area we cannot identify the event horizon. A fault terminated just below the event horizon, at a horizontal distance of ca. 6.25 m on the east wall of the trench, which might correspond to the event that formed the gravel wedge W5 although this was not conclusive. There was relatively little supporting evidence for this event horizon.

#### 5.3.4.5. *Paleoearthquake T3E4*

This event horizon was defined as the base of the gravel wedge W6, which had a similar geometry on the trench wall to that of the gravel wedges up-sequence. No fault terminations were recognized at this event horizon. The equivalent gravel units in and north of the fault zone cannot be correlated to the gravel wedge W6. This was attributed to lateral

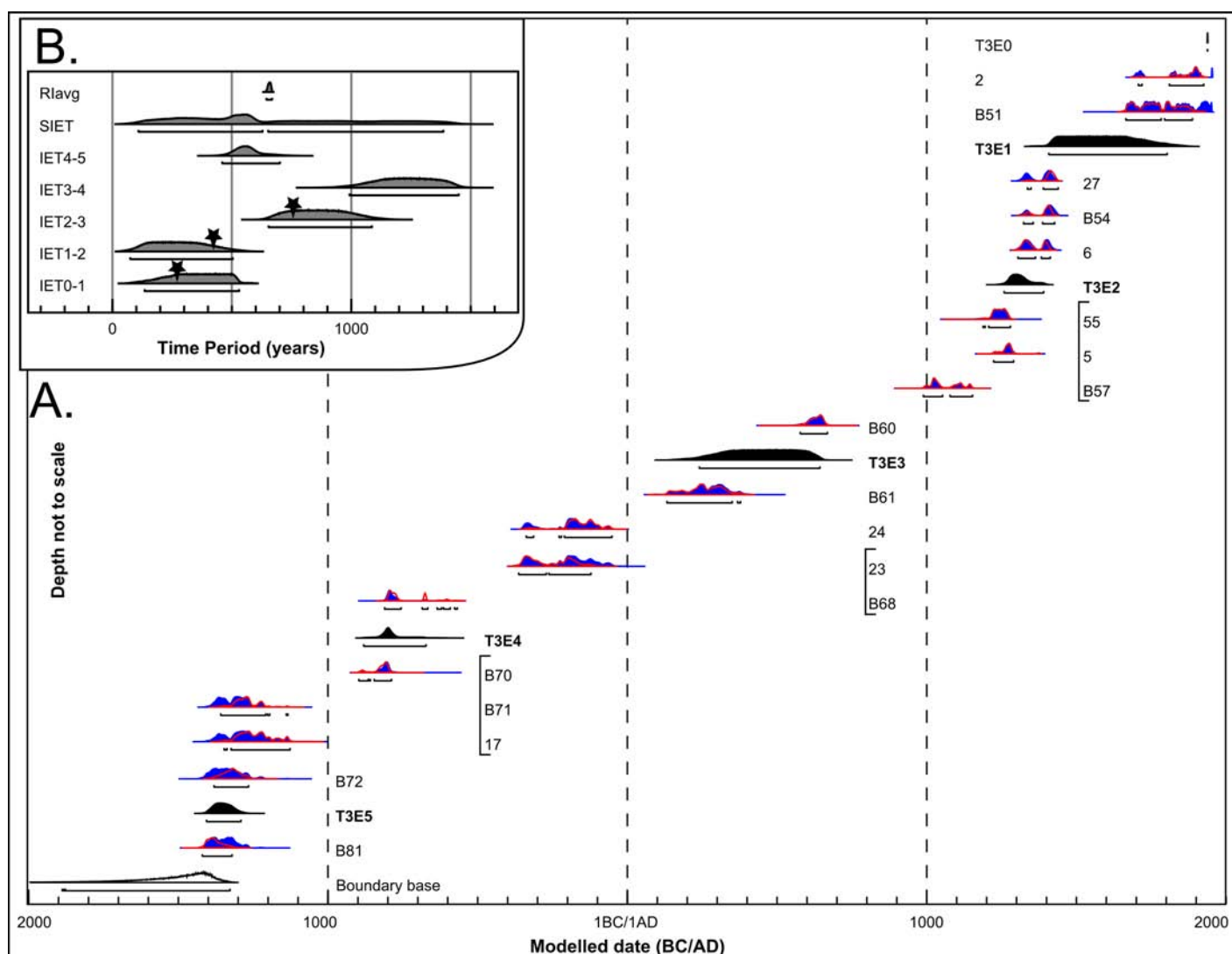


**Figure 9.** (a) Plot of the order-constrained Bayesian model (using OxCal software) [Bronk Ramsey 2007] constructed for trench T3, showing the calibrated sample age probability density functions (PDFs) (blue fill, no boundary), modeled sample age PDFs (no fill, red boundary), and earthquake age PDFs (black filled). Samples that are grouped into phases in the order-constrained Bayesian model (electronic supplement 1) are indicated with brackets. Samples were calibrated using the IntCal04 curve [Reimer et al. 2004]. T3E0 was entered into the model as a fixed date, corresponding to the Erzincan rupture in A.D. 1939. (b) Plot of the PDFs of the inter-event times (IETs) calculated using OxCal [Bronk Ramsey 2007]. PDFs labeled IET $n$ - $m$  correspond to individual IETs (i.e. IET0-1 is the IET between event E0 and event E1), SIET is the summed IET, and Rlavg is the average recurrence interval. Black stars show the IETs inferred from the correlated historical earthquakes.

offset, which is probably quite significant if four subsequent, predominantly strike-slip, surface-rupturing earthquakes occurred in this segment.

#### 5.3.4.6. Paleoseismicity T3E5

The evidence for this event was a colluvial wedge (the gravel wedge W7). This gravel wedge was somewhat smaller than many of the younger wedges, although it was the lowest wedge that was clearly discernible from the massive gravel Ga at the bottom of the trench. There was also no supporting tectonostratigraphic evidence for this event horizon.

Further validation of the evidence for the event horizons can be found by comparison of the ages with the events that were identified in paleoseismic trenches T1 and T2 and from the results from other paleoseismic studies undertaken for the nearby sections of the NAF.

## 6. Paleoseismicity timing

To constrain the age of the event horizons established using colluvial wedges in trench T3, we radiocarbon dated 16 charcoal samples and 14 bulk samples (Table A.B-1, Annex B). The bulk samples were processed to extract pollen, although at a late stage in the process we found that there was not enough pollen to use for the dating. Therefore, the dated materials comprised 40-63- $\mu$ m-sized organics that were dominated by micro charcoal and pollen fragments (see Annex B for a description of the processing procedure). As is common when many samples are dated in a sedimentary sequence, many of the sample ages were inconsistent with their relative stratigraphic positions [e.g. Hartleb et al. 2003, Fraser et al. 2009a, Fraser et al. 2010b]. It was difficult to distinguish between reliable and unreliable sample ages. However, a parsimonious approach was taken, whereby the least samples were

excluded to establish a stratigraphically logical sequence of sample ages. Eight samples were interpreted as too old relative to the adjacent sample ages. This was attributed to reworking of sample material from the southern face of the elongate linear ridge and alluvial fans and their catchments. Four of the samples were interpreted as too recent relative to the adjacent sample ages, which was attributed to bioturbation, although the fine-grained deposits might also be prone to desiccation cracking, which would provide conduits for organic material to be washed into the subsurface (i.e. creating an anomalously young age in the stratigraphic unit in which it is deposited).

Using the remaining 18 samples, we made an order-constrained Bayesian model (electronic supplement 1) using the OxCal software [Bronk Ramsey 2007] to derive the modeled probability density functions (PDFs) of the samples and the earthquake ages (Table 2, Figure 9). Where multiple samples from a stratigraphic unit were incorporated in the Bayesian model, they were grouped into 'phases' (relative order unspecified), and these phases were grouped into a sequence, along with the individual samples from the stratigraphic units (i.e. not in a 'phase'), according to their stratigraphic order. The order-constrained Bayesian model had a model index of 91 [Bronk Ramsey 2007], which exceeded the recommended 60 for a conformable model.

The order-constrained Bayesian model was also used to determine the PDFs of the inter-event times, the summed inter-event times, and the average recurrence intervals (Table 3, Figure 9b) (i.e. using the same methodology as Lienkaemper and Bronk Ramey [2009] and Fraser et al. [2010b]). The inter-event time is the period between two earthquakes expressed as a PDF that accounts for the uncertainty in the timings of the earthquakes. The summed inter-event time was the normalized sum of the inter-event times, and it provided a very good description of the probable time between the earthquakes, taking into account both the natural variation in recurrence interval and the uncertainty associated with constraining the age of earthquakes. The average recurrence interval was simply the period between the most recent (T3E0: 1939 Erzincan earthquake) and the oldest event (as a PDF), divided by the number of inter-event times, which in this case was 5.

The Bayesian model for trench T3 provided by far the best earthquake record of the three trenches, although the data were complementary to the findings of T1 and T2. Trench T1 showed us that one earthquake (T1E0) occurred after deposition of sample 37 (CRA: A.D. 1494 – A.D. 1951  $2\sigma$ ), which is consistent with trenches T2 and T3. Trench T2 showed us that two earthquakes occurred after ca. A.D. 1660, using only the highest two samples below two event horizons (T2E0 and T2E1). This is consistent with trench T3, where we interpreted the ultimate event as the 1939 Erzincan earthquake (Table 2), and the age of the penultimate event (T3E1) was constrained to between A.D. 1408 and A.D. 1804.

Variable	$2\sigma$ Age range (years)
IET0-1	135–530
IET1-2	75–504
IET2-3	654–1086
IET3-4	993–1450
IET4-5	460–701
SIET	109–1385 (bimodal)
RIavg	646–669

**Table 3.** Duration between earthquakes derived from the OxCal model (see Figure 9 and electronic supplement 1). Note: IET0-1 is the inter-event time between event 0 and event 1. SIET, summed inter-event time; RIavg, average recurrence interval.

The information from trench T2 strongly suggested that the penultimate event (T2E1) occurred between ca. A.D. 1660 and A.D. 1804. The third event horizon that was identified in trench T2 (T2E2) was constrained to some time between A.D. 200 and A.D. 1640, which is consistent with the event T3E2 (A.D. 1254 – A.D. 1391) from trench T3, although far less precise. The relatively good correlations between the three trenches provided some validation to the link between the formation of gravel wedges in trench T3 and the other types of evidence of paleoearthquakes revealed in trenches T1 and T2. The older paleoearthquakes determined in trench T3 are summarized in Table 2.

As event T3E0 corresponded to T2E0 and T1E0, and as T3E1 corresponded to T2E1, and so on, hereafter we refer to these events as E0, E1, E2, etc.

## 7. Spatiotemporal pattern of faulting

### 7.1. Fault-rupture correlation

This discussion focuses on comparing the earthquake record that was established in the present study (Table 2) to paleoearthquake chronologies from three other paleoseismic investigations on the 1939 Erzincan earthquake rupture segment and to the records of historical earthquakes (Table 1). The other paleoseismic sites (Figure 1b) were Resadiye [Fraser 2009b], which is located on the Kelkit Valley fault segment ca. 130 km west of Günealan, and Yaylabeli [Kozaci et al. 2011] and Cukurcimen [Hartleb et al. 2006], which are located near the eastern end of the Mihar–Tumekar fault segment that is 27 km and 31 km east of Günealan, respectively. Table 4 summarizes the correlations that are presented graphically in Figure 10.

To use paleoearthquake timing data to investigate whether previous earthquakes had the same extent of fault rupture as the 1939 Erzincan earthquake, two assumptions were made:

1. Where paleoearthquakes were dated to around the same time at multiple locations on the fault rupture segment,

Resadiye [Fraser 2009b]	Günalan [the present study]	Yaylabeli [Kozaci et al. 2011]	Cukurcimen [Hartleb et al. 2006]	Historical Earthquakes (See Table 4)
Event 0 unconstrained	E0 unconstrained	E1 A.D. 1150–A.D. 1939	Event A unconstrained	A.D. 1939 Erzincan earthquake
Event 1 A.D. 1570–A.D. 1939	E1 A.D. 1408–A.D. 1804	—	—	A.D. 1668 ?
—	E2 A.D. 1259–A.D. 1391	E2 A.D. 1150–A.D. 1939	Event B A.D. 980–A.D. 1420	A.D. 1254
—	—	E3 A.D. 910–A.D. 1110	Event C A.D. 930–A.D. 1070	A.D. 1045
—	—	E4 A.D. 710–A.D. 850	—	—
Event 2 A.D. 262–A.D. 642	E3 A.D. 241–A.D. 644	E5 A.D. 320–A.D. 690	Event D A.D. 360–A.D. 540	A.D. 499
Event 3 258 B.C.–A.D. 206	—	X	Event E 230 B.C.–A.D. 50	—
Event 4 908 B.C.–702 B.C.	E4 881 B.C.–673 B.C.	X	Possibly Event F 1450 B.C.–800 B.C.	—
—	E5 1406 B.C.–1291 B.C.	X	Possibly Event F 1450 B.C.–800 B.C.	1200 B.C.
Event 5 2020 B.C.–1804 B.C.	X	X	X	—
Event 6 2280 B.C.–2066 B.C.	X	X	X	—
— Earthquake not recognized				
X Older than exposed earthquake record				

**Table 4.** Earthquake timing comparison with nearby paleoseismic studies on the NAF and correlated historical earthquakes (historical earthquake records are summarized in Table 1), summarized graphically in Figure 10. Note: '—' corresponds to 'earthquake not recognised' and 'X' corresponds to 'older than exposed in earthquake record'.

they reflect a single earthquake. However, this assumption might erroneously group surface-rupturing earthquakes that occur closely spaced in time (relative to the age constraint determined in paleoseismic investigations).

2. Where paleoearthquakes were not present in the stratigraphy at one location, but they were at others, then only part of the fault-rupture segment ruptured. This assumption might be erroneous where the paleoseismic investigation provides an incomplete paleoearthquake record; this is very difficult to prove or disprove.

All of the paleoseismic studies on the 1939 rupture segment have recognizable evidence of the 1939 Erzincan earthquake [Hartleb et al. 2006, Fraser 2009b, Kozaci et al. 2011], which is consistent with the extent of the fault rupture segment that was described by Barka [1996]. In the present study, the 1939 earthquake was interpreted to correspond to E0, although due to the imprecision of radiocarbon dating in

the last few hundred years, this must remain an assumption.

In trench T3, event E1 was constrained to A.D. 1408 – A.D. 1804, which corresponds to the timing of 10 possible historical earthquakes (Table 1). However, Trench T2 indicated that this event occurred after ca. A.D. 1660, which reduces the possible correlative events to earthquakes in A.D. 1668, 1684, and 1754 (Table 1). This event was interpreted to correlate to one of the three major earthquakes that were reported in A.D. 1668 [Ambraseys and Finkel 1995, Ambraseys and Jackson 1998, Sengor et al. 2005], due to the likely extensive rupture that was associated with these events. However, with the data from the present study, it is possible that this evidence was associated with the historical reports of earthquakes in A.D. 1684 or A.D. 1754. This earthquake was also recognized at Resadiye [Fraser 2009b], but not in the trenches to the east of the present study [Hartleb et al. 2006, Kozaci et al. 2011]. This suggests that the Mihar–Tumekar fault segment (Figure



Of note, there was a long period of time between the A.D. 499 (E3) earthquake and the subsequent earthquake (E2) in A.D. 1254 recognized at Günalan. Over that period, no earthquakes were recognized at Resadiye [Fraser 2009b], whereas the two studies to the east both recognized an earthquake in A.D. 1045 [Hartleb et al. 2006, Kozaci et al. 2011], and another event was recognized at Yaylabeli for A.D. 710 – A.D. 850 [Kozaci et al. 2011]. Again, this suggests that there is a fault rupture segmentation boundary between Günalan and Yaylabeli. Alternatively, it is possible that these events were spillover displacements from the Erzincan fault segment (Figure 1c).

Event E4 was constrained to the period 881 B.C. – 673 B.C., which does not correlate to any earthquakes in the historical record. Event E4 corresponds to an earthquake identified at Resadiye that was constrained to the period 908 B.C. – 702 B.C. [Fraser 2009b], although the paleoseismic record from Yaylabeli [Kozaci et al. 2011] did not extend beyond the A.D. 499 earthquake. The Cukurcimen study identified an event at 1450 B.C. – 800 B.C., which might correspond to this event, although the large age bracket overlaps more with the timing of E5.

Between events E3 and E4, there was an event identified both west of our trenching site at Resadiye [Fraser 2009b] and to the east at Cukurcimen [Hartleb et al. 2006] (Table 1). The absence of this event in trench T3 suggested that either this paleoearthquake did rupture the fault at Günalan and no evidence was preserved in our trench, or that it corresponded to two separate paleoearthquakes that occurred at around the same period on each end of the 1939 rupture segments.

Event E5 (1406 B.C. – 1291 B.C.) was interpreted to correspond to the oldest event identified at Cukurcimen [Hartleb et al. 2006]. Although the  $2\sigma$  range of E5 does not overlap with 1200 B.C., this event might correspond to an earthquake, or series of earthquakes (like that of the 20th Century), that might have occurred ca. 1200 B.C. [Nur and Cline 2000]. The occurrence, timing, and extent of damage associated with this earthquake is relatively speculative and is based on archeological evidence. This event was not identified at Resadiye [Fraser 2009b], which suggested that the earthquake fault rupture stopped somewhere between Günalan and Resadiye. Of note, the paleoseismic record at Resadiye identified two older earthquakes (Table 4)

Figure 9b presents the inter-event times (IETs), which are summarized in Table 3. IET0-1 corresponds to the interval between events E0 and E1, IET1-2 to the interval between event E1 and E2, and so on. If our correlations of paleoearthquakes to historical earthquakes are correct, then IET0-1 is 271 years, IET1-2 is 414 years, and IET2-3 is 755 years; the older events were not matched to historical earthquakes. These correlative IETs fall within the IET PDFs determined from our paleoseismic data. The summed IET (SIET) calculated using only paleoseismic data from Günalan

had a broad  $2\sigma$  range of 109 years to 1385 years, which is very similar to the 0 years to 1375 years determined at Resadiye [Fraser 2009b]. The SIET at Resadiye [Fraser 2009b] was found to be bimodal, with modes at 100 years to 400 years, and at 900 years to 1200 years, which was speculatively attributed to two typical-sized earthquakes that ruptured the Kelkit Valley segment of the NAF. At Günalan, there was also bimodality or multimodality. The longer SIET mode is due to two long IETs, between E2 and E3, and between E3 and E4. This suggests a relatively variable period between large earthquakes. Fraser et al. [2010a] use these data along with order-constrained Bayesian models for paleoseismic investigations along the entire NAF, to investigate the spatial and temporal patterns of paleoearthquakes.

### 7.2. Paleoseismicity magnitude estimations

Assuming that the paleoseismic investigations identified a continuous (complete) record of earthquakes locally, the fault segments that comprised the 1939 Erzincan earthquake fault-rupture segment do not always rupture in tandem. By roughly estimating the length of the fault rupture associated with paleoearthquakes, we can estimate their magnitude. Figure 10 summarizes the lengths of the ruptures associated with the paleoearthquakes described in the previous section and summarized in Table 4.

Using the length of rupture of the paleoearthquakes based on paleoseismic investigations and the fault segmentation proposed by Barka [1996], we estimated the lengths of rupture for the paleoearthquakes correlated between the investigation sites in Table 4. We used an empirical equation ( $M_w = A + B \log L$ ) that relates the length of rupture ( $L$ ) and regression coefficients ( $A$ , Y-axis intercept;  $B$ , regression slope) to moment magnitude ( $M_w$ ) [Wells and Coppersmith 1994]. We estimated the  $M_w$  of the paleoearthquakes and the rupture of the individual fault segments proposed by Barka [1996]. The  $1\sigma$  limits of the regression coefficients ( $A = 5.16 \pm 0.13(1\sigma)$ ,  $B = 1.12 \pm 0.08(1\sigma)$ ) provided by Wells and Coppersmith [1994] were used to estimate the maximum and minimum moment magnitudes. These estimates assume that the fault segment boundaries identified by Barka [1996] were valid in most cases. The magnitudes estimated for the possible fault-rupture segment lengths associated with the paleoearthquakes (as summarized in Table 5) all exceeded  $M_w$  7.0, which suggests that these shorter ruptures along the 1939 Erzincan earthquake rupture segment also produce large magnitude earthquakes.

### 7.3. Fault-rupture cycles

Figure 10 graphically summarizes the rupture lengths and our estimated magnitudes. An important observation is that we did not recognize a cyclical pattern of earthquakes. The number of paleoseismic studies along the 1939 fault-rupture segment is not great enough to draw any definitive con-

Event	Event number [present study]	Segments ruptured <sup>a</sup>	Total length of rupture (km)	Magnitude estimate (Mw) <sup>b</sup>	
				Minimum	Maximum
<b>Individual fault segments</b>					
schematic	-	A	90	7.1	7.6
schematic	-	B	100	7.1	7.7
schematic	-	C	45	6.7	7.3
schematic	-	D	65	6.9	7.5
schematic	-	E	60	6.9	7.4
<b>Scenarios</b>					
A.D. 1939	E0	A, B, C, D, E	350	7.7	8.3
A.D. 1668	E1	A, B, C, D,	250	7.6	8.3
A.D. 1254	E2	D, E	170	7.2	7.8
A.D. 1045	Not observed	D (partial) , E	100	7.1	7.7
A.D. 499	E3	A, B, C, D, E	360	7.7	8.4
250 B.C. - A.D. 100	Not observed	unsure			
900 B.C. - 700 B.C.	E4	A, B, C, D, E	360	7.7	8.4
ca. 1200 B.C.	E5	D, E (?)	170	7.2	7.8

**Table 5.** Earthquake magnitude estimates for a range of rupture lengths. Note <sup>a</sup>, letters correspond to fault segments shown on Figure 1: A, Ezinepazari; B, Kelkit Valley; C, Ortakoy–Susehri; D, Mihar–Tumekar; E, Erzincan. Note <sup>b</sup>, magnitude estimated using formula and regression coefficients from Wells and Coppersmith [1994]; see text for description.

clusions. Further studies are required, particularly on the Ezinepazari, Ortakoy–Susehri and Erzincan fault segments. However, the interpretation of the results from the paleoseismic investigation that are plotted in Figure 10 suggests that the eastern fault segments of the 1939 Erzincan earthquake fault-rupture segment have a shorter recurrence interval (i.e. more frequent earthquakes).

Sieh [1996] described fault segments (map-views) as 'patches', in terms of a three-dimensional section of a fault plane. He documented examples where, "adjacent individual patches, 10 km or more in length, failed singly during one event and in tandem during the other", and found that, "...large earthquakes commonly result from the failure of one or more patches, each characterized by a slip function that is roughly invariant through consecutive cycles" [Sieh 1996, p. 3764], with the exception of transition zones between slip patches, where the slip might deviate from event to event. With the data available from the paleoseismic studies along the 1939 Erzincan earthquake rupture segment, we cannot determine if any of the sites are at the transition zones between slip patches. It would therefore be advantageous to know the amount of slip during the paleoearthquakes along the 1939 rupture segment.

Fraser et al. [2010a] described the behavior of the eastern sections of the NAF as bimodal, with two apparent typical periods between paleoearthquakes. The variable times between earthquakes, the time-variable fault rupture lengths, and hence the variable earthquake magnitudes might be due to the intermittent effects of contagion. Fault-rupture contagion is where the rupture of one fault or fault segment in-

creases the likelihood of the occurrence of the rupture of an adjacent fault or fault segment [Perkins 1987]. As Perkins [1987, p. 429] noted: "Under certain conditions, the [fault] system can behave as a two-stage process: one stage having a high recurrence rate [i.e. frequent earthquakes] during the contagion processes and a second stage having a long, quiescent inter-contagion time". In the case of the 1939 fault-rupture segment, contagion might be associated with the adjacent fault segments of the NAF or from other faults. By investigating spatiotemporal patterns of seismicity using paleoseismic data from southern California, Dolan et al. [2007] showed that seismicity of one fault system can suppress seismicity of another fault system that accommodates the same plate boundary motion. Such a relationship between the NAF and, for example, one or a combination of the East Anatolian Fault, the Northeast Anatolian Fault, the Ovacik Fault, and/or the Almus Fault (Figure 1a), or of other faults, might affect the spatiotemporal distribution of earthquakes on the eastern section of the NAF [Fraser et al. 2010a]. This can also be considered in terms of stress transfer. Stein et al. [1997] showed that stress changes induced by fault rupture of adjacent fault strands, or of other faults, can increase the likelihood of rupture on a particular section of the NAF.

Barka [1996, p. 1240] noted that, "The 20 November 1939 Tercan earthquake, an  $M = 5.9$  event that occurred 5 weeks before the 1939 Erzincan earthquake on the NE-SW striking Northeast Anatolian Fault, is considered to be a preshock [sic] of the 1939 Erzincan earthquake". This suggested that there might be some degree of behavioral coupling between these fault systems in terms of triggering, but

it does not provide evidence of coupling in terms of long-term behavior. To address this further, studies on adjacent fault systems such as the Northeast Anatolian Fault, Almus Fault and Ovacik Fault are required to provide long records of paleoearthquakes.

## 8. Conclusions

A paleoseismic investigation was undertaken of the 1939 Erzincan earthquake rupture segment of the NAF near the village of Günalan, between the pre-existing investigations at Resadiye [Fraser et al. 2009b] to the west, and at Yaylabeli [Kozaci et al. 2011] and Cukurcimen [Hartleb et al. 2006] to the east. The present investigation comprised three paleoseismic trenches. Trenches T1 and T2 were excavated on the alluvial plain of the Cobanlı River. Trench T1 revealed clear evidence for one earthquake after ca. A.D. 1494, which was interpreted as the 1939 Erzincan earthquake. Trench T2 revealed evidence of two earthquakes near the top of the trench, both of which occurred sometime after ca. A.D. 1660, and one of which was interpreted as the 1939 Erzincan earthquake. A third event in trench T2 was constrained to A.D. 200 – A.D. 1640. Trench T3 revealed a record of colluvial gravel wedges that interfingered with fine-grained inter-fan deposits. We interpreted a sequence of six earthquake event horizons here, including the 1939 Erzincan earthquake. Using 18 of the 30 radiocarbon dated samples, a Bayesian ordering-constrained model was used to constrain the ages of the six event horizons. The penultimate earthquake (E1) was constrained to A.D. 1408 – A.D. 1804 in trench T3, while data from trench T2 suggested that this earthquake occurred after ca. A.D. 1660. We correlated this event to the historical A.D. 1668 earthquake. The antepenultimate earthquake (E2) was constrained to A.D. 1259 – A.D. 1391 and was correlated to the historical A.D. 1254 earthquake. The fourth earthquake in the sequence (E3) was constrained to A.D. 241 – A.D. 644, which was correlated to the historical earthquake in A.D. 499. Event E4 occurred during 881 B.C. – 673 B.C. and cannot be matched to a historical earthquake. Event E5, which was the oldest earthquake recognized at Günalan, occurred during 1406 B.C. – 1291 B.C., which might correlate to a sequence of earthquakes that might have occurred around 1200 B.C.

By comparing the earthquake timing data from this study to the results of other paleoseismic studies of the 1939 Erzincan earthquake rupture segment, it appears that this section of the NAF does not always rupture in unison. The A.D. 1668 earthquake appears to have ruptured a western portion of the 1939 rupture segment, with the eastern rupture termination located between Günalan and the paleoseismic investigation site at Yaylabeli. The A.D. 1254 earthquake appears to have ruptured an eastern portion of the 1939 rupture segment, with the western termination of the rupture occurring between Resadiye and Günalan. Earth-

quakes in A.D. 1045 and from A.D. 710 to A.D. 1050 were encountered in paleoseismic investigations to the east of Günalan. The A.D. 499 earthquake was recognized in all of the paleoseismic investigations along the 1939 earthquake rupture segment, and therefore we suggest that this earthquake was similar to the 1939 earthquake. An earthquake between 250 B.C. and A.D. 100 was encountered at Resadiye and Cukurcimen, to the west and east of Günalan, respectively. This might reflect one earthquake that was not revealed at Günalan, or it might reflect two separate earthquakes that occurred within a period of several hundred years. An earthquake that occurred around 900 B.C. to 700 B.C. appears to have ruptured most, if not all, of the 1939 Erzincan earthquake fault-rupture segment, like the A.D. 499 event. An earthquake around 1200 B.C. might have had a similar rupture pattern as the A.D. 1254 earthquake.

The pattern of the earthquakes revealed by this comparison with the paleoseismic investigation data along the 1939 Erzincan earthquake rupture segment indicates that this section of the NAF does not behave in the same way during each seismic cycle, which has resulted in earthquakes of different, but still large, magnitudes. The time-variable fault-rupture lengths are likely to be due to contagion, which might have come from one or more sources.

**Acknowledgements.** We acknowledge the European Commission for funding this project as part of the Marie Curie Excellence Grant Project *Understanding the irregularity of seismic cycles: A case study in Turkey* (MEXT-CT-2005-025617: Seismic Cycles). We would like to thank the local people and authorities of the Golova area for their hospitality, and for allowing us to conduct our investigations. We would like to thank the people of Susehri, where we stayed during the field work, for their kind hospitality, especially Jabba, who showed us great friendship. Thanks also go to C. Ballard, M. Meghraoui and F. Cinti for reviewing this manuscript and for providing useful comments.

## References

- Ambraseys, N.N. (1970). Some characteristic features of the Anatolian fault zone, *Tectonophysics*, 9, 143-165.
- Ambraseys, N.N., and C.F. Finkel (1995). *The Seismicity of Turkey and Adjacent Areas: A Historical Review, 1500-1800*, Muhittin Salih Eren, Istanbul, Turkey, 240 pp.
- Ambraseys, N.N., and J. Jackson (1998). Faulting associated with historical and recent earthquakes in the eastern Mediterranean region, *Geophys. J. Intl.*, 133, 390-406.
- Anderson, J.G., S.G. Wesnousky and M.W. Stirling (1996). Earthquake size as a function of fault slip rate, *B. Seismol. Soc. Am.*, 86, 683-690.
- Armijo, R., B. Meyer, A. Hubert and A. Barka (1999). Westward propagation of the North Anatolian Fault into the northern Aegean: timing and kinematics, *Geology*, 27, 267-270.
- Barka, A.A. (1992). The North Anatolian fault zone, *Annales Tectonicae*, 6, 164-195.
- Barka, A. (1996). Slip distribution along the North Anatolian Fault associated with the large earthquakes of the period

- 1939 to 1967, *B. Seismol. Soc. Am.*, 86, 1238-1254.
- Barka, A.A., S.H. Akyuz, H.A. Cohen, and F. Watchorn (2000). Tectonic evolution of the Nixsar and Tasova-Erbaa pull-apart basins, North Anatolian Fault Zone: their significance for the motion of the Anatolian block, *Tectonophysics*, 322, 243-264.
- Barka, A., H. Akyuz, E. Altunel, G. Sunal, Z. Cakir, A. Dikbas, B. Yerli, R. Armijo, B. Meyer, and J. de Chabaliere (2002). The Surface Rupture and Slip Distribution of the 17 August 1999 Izmit Earthquake (M 7.4), North Anatolian Fault, *B. Seismol. Soc. Am.*, 92, 43-60.
- Biasi, G., and R. Weldon (1994). Quantitative refinement of calibrated C-14 distributions, *Quaternary Research*, 41, 1-18.
- Biasi, G.P., R.J. Weldon, T.E. Fumal and G.G. Seitz (2002). Paleoseismic event dating and the conditional probability of large earthquakes on the southern San Andreas Fault, California, *B. Seismol. Soc. Am.*, 92, 2761-2781.
- Bronk Ramsey, C. (2007). OxCal Program v. 4.0.5, Radiocarbon Accelerator unit, University of Oxford, UK; <https://c14.arch.ox.ac.uk/oxcal.html>
- Dolan, J., F.D. Bowman and C. Sammis (2007). Long range and long-term fault interactions in southern California, *Geology*, 35 (9), 855-858; doi:10.1130/G23789A.1.
- Flerit, F., R. Armijo, G. King and B. Meyer (2004). The mechanical interaction between the propagating North Anatolian Fault and the back-arc extension in the Aegean, *Earth and Planetary Science Letters*, 224, 347-362; doi:10.1016/j.epsl.2004.05.028
- Fraser, J.G., J.S. Pigati, A. Hubert-Ferrari, K. Vanneste, U. Avsar and S. Altinok (2009a). A 3000-year record of ground-rupturing earthquakes along the central North Anatolian Fault near Lake Ladik, Turkey, *B. Seismol. Soc. Am.*, 99; doi:10.1785/0120080024.
- Fraser, J.G. (2009b). Four new paleoseismic investigations on the North Anatolian Fault, Turkey, in the context of existing data, Ph.D. thesis, Univ. Libre de Bruxelles, Belgium, Brussels, 284 pp.
- Fraser, J.G., K. Vanneste and A. Hubert-Ferrari (2010a). Recent behavior of the North Anatolian Fault: Insights from an integrated paleoseismological data set, *J. Geophys. Res.*, 115, B09316; doi:10.1029/2009JB006982.
- Fraser, J.G., A. Hubert-Ferrari, K. Vanneste, S. Altinok and L. Drab (2010b). A relict sedimentary record of seven earthquakes between 600 AD and 2000 BC on the central North Anatolian Fault at Elmacik, near Osmancik, Turkey, *Geol. Soc. Am. Bull.*, 122, 1830-1845; doi:10.1130/B30081.1.
- Guidoboni, E., A. Comastri and G. Traina (1994). Catalogue of ancient earthquakes in the Mediterranean area up to the 10th century, Istituto Nazionale di Geofisica, Rome, 504 pp.
- Guidoboni, E., and A. Comastri, eds. (2005). Catalogue of earthquakes and tsunamis in the mediterranean area from the 11th to the 15th century, Istituto Nazionale di Geofisica e Vulcanologia, Bologna, 1037 pp.
- Gulen, L., A. Pinar, D. Kalafat, N. Ozel, G. Horasan and M. Yilmazer (2002). Surface Fault Breaks, Aftershock Distribution, and Rupture Process of the 17 August 1999 Izmit, Turkey, Earthquake, *B. Seismol. Soc. Am.*, 92, 230-244.
- Hartleb, R.D., J.F. Dolan, H.S. Akyuz and B. Yerli (2003). A 2000-Year-Long Paleoseismologic Record of Earthquakes along the Central North Anatolian Fault, from Trenches at Alayurt, Turkey, *B. Seismol. Soc. Am.*, 93, 1935-1954.
- Hartleb, R.D., J.F. Dolan, O. Kozaci, H.S. Akyuz and G.G. Seitz (2006). A 2500-yr-long paleoseismologic record of large, infrequent earthquakes on the North Anatolian fault at Cukurcimen, Turkey, *B. Seismol. Soc. Am.*, 118, 823-840; doi:10.1130/B25838.1.
- Hilley, G.E., and J.J. Young (2008a). Deducing Paleoearthquake Timing and Recurrence from Paleoseismic Data, Part I: Evaluation of New Bayesian Markov-Chain Monte Carlo Simulation Methods Applied to Excavations with Continuous Peat Growth, *B. Seismol. Soc. Am.*, 98; doi:10.1785/0120020077.
- Hilley, G.E., and J.J. Young (2008b). Deducing Paleoearthquake Timing and Recurrence from Paleoseismic Data, Part II: Analysis of Paleoseismic Excavation Data and Earthquake Behavior along the Central and Southern San Andreas Fault, *B. Seismol. Soc. Am.*, 98; doi:10.1785/0120070012.
- Hubert-Ferrari, A., R. Armijo, G. King, B. Meyer and A. Barka (2002). Morphology, displacement, and slip rates along the North Anatolian Fault, Turkey, *J. Geophys. Res.*, 107; doi:10.1029/2001JB000393.
- Hubert-Ferrari, A., G. King, J. Van der Woerd, I. Villa, E. Altunel and E. Armijo (2009). Long-term evolution of the North Anatolian Fault: new constraints from its eastern termination, Collision and Collapse at the Africa-Arabia-Eurasia Subduction Zone, The Geological Society, London, Special Publications, vol. 311, edited by D.J.J. Van Hinsbergen, M.A. Edwards and R. Govers, pp. 133-154; doi: 10.1144/SP311.5.
- Keefer, D.K. (1984). Landslides caused by earthquakes, *B. Seismol. Soc. Am.*, 95, 406-421.
- Koçyiğit, A. (1989). Susehri basin: an active fault-wedge basin on the North Anatolian Fault Zone, Turkey, *Tectonophysics*, 167, 13-29.
- Koçyiğit, A. (1990). Tectonic setting of the Golova basin: Total offset of the North Anatolian Fault zone, E Pontide, Turkey, *Annales Tectonicae*, 2, 155-170.
- Kozaci, O., J.F. Dolan, O. Yonlu and R.D. Hartleb (2011). Paleoseismologic evidence for the relatively regular recurrence of infrequent, large-magnitude earthquakes on the eastern North Anatolian fault at Yaylabeli, Turkey, *Lithosphere*, 3, 37-54; doi:10.1130/L118.1.
- Lienkaemper, J.J., and C. Bronk Ramey (2009). OxCal: Versatile tool for developing paleoearthquake chronologies

- a primer, *Seismol. Res. Lett.*, 80, 431-434; doi:10.1785/gssrl.80.3.431
- Nur, A., and E.H. Cline (2000). Poseidon's horses: Plate tectonics and earthquake storms in the Late Bronze Age Aegean and Eastern Mediterranean, *Journal of Archaeological Science*, 27, 43-63.
- Okumura, K., T. Yoshioka and I. Kusu (1994). Surface faulting on the North Anatolian Fault in these two millennia, Proceedings of the workshop on paleoseismology, USGS, Menlo Park, California, Open-File Report 94-568, 143-144.
- Perkins, D.M. (1987). Contagious fault rupture, probabilistic hazard, and contagion observability, In: A.J. Crone and E.M. Omdahl (eds.), Conference proceedings: Directions in Paleoseismology, US Geol. Surv., Open file report 87-673, 428-439.
- Pondard, N., R. Armijo, G.C. P. King, B. Meyer, and F. Flerit (2007). Fault interactions in the Sea of Marmara pull-apart (North Anatolian Fault): earthquake clustering and propagating earthquake sequences, *Geophys. J. Int.*, 171, 1185-1197; doi:10.1111/j.1365-246x.2007.03580.x.
- Reilinger, R., S. McClusky, P. Vernant, S. Lawrence, S. Ergintav, R. Cakmak, H. Ozener, F. Kadirov, I. Guliev, R. Stepanyan, M. Nadariya, G. Hahubia, S. Mahmoud, K. Sakr, A. ArRajehi, D. Paradissis, A. Al-Aydrus, M. Prilepin, T. Guseva, E. Evren, A. Dmitrotsa, S. V. Filikov, F. Gomez, R. Al-Ghazzi and G. Karam (2006). GPS constraints on continental deformation in the Africa-Arabia-Eurasia continental collision zone and implications for the dynamics of plate interactions, *J. Geophys. Res.*, 111; doi:10.1029/2005JB004051.
- Reimer, P.J., M.G.L. Baillie, E. Bard, A. Bayliss, J.W. Beck, C.J.H. Bertrand, P.G. Blackwell, C.E. Buck, G.S. Burr, K.B. Cutler, P.E. Damon, R.L. Edwards, R.G. Fairbanks, M. Friedrich, T.P. Guilderson, A.G. Hogg, K.A. Hughen, B. Kromer, F.G. McCormack, S.W. Manning, C.B. Ramsey, R.W. Reimer, S. Remmele, J.R. Southon, M. Stuiver, S. Talamo, F.W. Taylor, J. Van Der Plicht and C.E. Weyhenmeyer (2004). IntCal04 terrestrial radiocarbon age calibration, 0-26 Ka cal BP, *Radiocarbon*, 46, 1029-1058.
- Sieh, K. (1996). The repetition of large earthquake ruptures, *Proc. Natl. Acad. Sci. U.S.A.*, 93, 3764-3771; doi:10.1073/pnas.93.9.3764.
- Sengor, A.M.C., N. Gorur and F. Saroglu (1985). Strike-slip faulting and related basin formation in zones of tectonic escape: Turkey as a case study, *Strike-slip faulting and basin formation*, Society of Economic Paleontologists and Mineralogists Special Publication No. 37, edited by: K.T. Biddle and N. Christie-Blick, Society of Economic Paleontologists and Mineralogists, Tulsa, Oklahoma, 227-264.
- Sengor, A., O. Tuysuz, C. Imren, M. Sakinc, H. Eyidogan, N. Gorur, X. Le Pichon and C. Rangin (2005). The North Anatolian Fault: A New Look, *Annu. Rev. Earth .Pl. Sc.*, 33, 37-112; doi:10.1146/annurev.earth.32.101802.120415.
- Stein, R.S., A.A. Barka and J.H. Dieterich (1997). Progressive failure on the North Anatolian fault since 1939 by earthquake stress triggering, *Geophys. J. Int.*, 128, 594-604.
- Stuiver, M., and H.A. Polach (1977). Reporting of <sup>14</sup>C Data, *Radiocarbon*, 19, 355-363.
- Wells, D.L., and K.J. Coppersmith (1994). New empirical relationships among magnitude, rupture length, rupture width, rupture area, and surface displacement, *B. Seismol. Soc. Am.*, 84, 974-1002.
- Wesnousky, S.G. (2006). Predicting the endpoints of earthquake ruptures, *Nature*, 444, 358-360; doi:10.1038/nature05275.
- Zabci, C., V. Karabacak, T. Sancar, H.S. Akyuz, E. Altunel, H. Gursoy and O. Tatar (2008). The possible eastward continuation of the 17 August 1668 Anatolian Earthquake on the North Anatolian Fault (NAF), Turkey, *Geophysical research Abstracts*, 10, abstract 05542.

---

\*Corresponding author: Jeff Fraser,  
now at Golder Associates New Zealand, Christchurch, New Zealand;  
email: jeph4e@gmail.com.

## ANNEX A. Stratigraphic unit descriptions

Symbol	Unit description
Topsoil	Brown sandy SILT with high organic content.
S1	Grey SAND and silty SAND planar and cross-bedded laminated in places. Contains some thin pebbly horizons particularly near the base.
S2	Grey silty SAND finely laminated with cross bedding.
S3	Undifferentiated S2 and S4.
S4	Beige silty SAND, clayey at some points.
C1	Beige silty CLAY.
Ps1	Dark brown SILT. Buried A horizon – Paleosol.
C2	Beige silty CLAY.
F1	Brown clayey SILT. Lower boundary with F2 is gradational.
F2	Gray gravely silty CLAY. Upper boundary with F1 is gradational.
Ps2	Dark brown SILT. Buried A horizon – Paleosol. On the east wall this unit has a lens of unit3 around which it grades laterally into unit C4.
C3	Light brown silty gravelly CLAY.
C4	Brown CLAY. Not present on the west wall. Probably altered Ps2 due to interaction with the water table.
C5	Light brown CLAY with occasional gravel clasts. Grades into blue gray CLAY to the south on the east wall – probably due to interaction with the water table.
Ps3	Dark brown SILT. Buried A horizon – Paleosol.
C6	Light brown CLAY with occasional gravel clasts, contains more gravel near the fault. Only present north of the fault zone on the east wall.
C7	Light brown CLAY. Only present north of the fault zone on the east wall.
Gx1	Beige clayey GRAVEL.
Gx2	Gray GRAVEL with clay coating – no matrix.
Gx3	Gray sandy GRAVEL with some imbrication.
Fz	Shear zone mixed materials with a fabric semi parallel to adjacent fault(s).
Cx	Light Brown CLAY – This generic label has been generated as we do not know which clay-rich unit this correlates to.

**Table A.A-1.** Paleoseismic trench T1: trench log stratigraphic unit descriptions. Symbols used on Figures 3 and 4.

Symbol	Unit Descriptions
Topsoil	Brown sandy SILT with high organic content.
S1	Brownish gray, silty SAND
S2	Pale brown silty fine SAND. In and north of the fault zone contains some gravel layers.
S3	Undifferentiated S2 and S4
S4	Grayish brown silty fine SAND
S5	Undifferentiated S2, S4, and S6
S6	Pale brown silty fine SAND
S7	Grayish brown silty fine SAND
S8	Pale yellowish brown, silty fine SAND. Near horizontal 13 contains some lenses of coarse sand. In and north of the fault zone contains some gravel layers.
I1	Pale brown laminated SAND. Not present on the east wall.
I2	Pale brown silty CLAY. Not present on the east wall.
I3 (g)	This unit is comprised of material similar to unit S8 in the upper half and a mixture of unit Ps1, Ps2 and S8 in the bottom half. Two of the subunits in this infill, denoted with a "g" contain abundant gastropod fragments. Not present on the west wall.
G1	Gray brown, silty sandy GRAVEL. In some places this unit is bedded with gravel-rich beds, in others it is well mixed.
Ps1a	Purple brown SILT. A buried A horizon – Paleosol.
G2	Gray brown, silty sandy GRAVEL. Very localized and only present on the east wall.
Ps1b	Grayish brown silty SAND with some oxide nodules. A buried B horizon – Paleosol. On both walls, in the fault zone and north of the fault zone the lower part of this unit has obvious liquefaction features and much of this unit may owe its origin to this source. It is unlikely that there was co-seismic sedimentation that was not associated with the earthquake.
Ps2a	Red brown gravelly sandy clayey SILT with some gravel. PS2# denotes 3 interesting features. The top area is disturbed and slightly darker. The middle area is rich in oxide nodules. The bottom area is silty sand. These three features appear to be related to bioturbation.
Ps2b	Brown silty sand GRAVEL.
S9	Greenish brown silty SAND.
S10	Brown silty fine SAND.
S11	Grayish brown, clayey medium SAND.
S12	Brown clayey silty fine SAND.
F1	Brown silty CLAY. More greenish brown on the east wall. F1# denotes 3 lenses within unit F1. The northern lens is comprised of coarse SAND, and the middle and southern lens are fine sand.
F2	Blue gray CLAY.
F3	Light reddish brown sand SILT. More light brown on the east wall.
G3	Gray brown silty GRAVEL. Not present of the west wall.
L1	Graying brown pebbly silty SAND. (liquefaction deposit)
L2	Grayish brown silty pebbly SAND. (liquefaction deposit)

**Table A.A-2.** Paleoseismic trench T2: trench log stratigraphic unit descriptions. Symbols used on Figures 5 and 6.

Symbol	Description
<b>South of the fault</b>	
Topsoil	Dark brown SILT with some pebbles – gravels.
W1	Brown gravelly pebbly SILT grading upwards into silty pebbly GRAVEL, grain sizes vary N-S within unit.
S1	Orange brown fine SAND, thin and discontinuous on the east wall.
W2	Dark brown silty GRAVEL, not recognized on the east wall. Becomes less gravelly away from the fault.
Ps1	Dark gray SILT, columnar soil structure, Paleosol.
F1	Dark red brown, silty CLAY, columnar soil structure, not recognized on the west wall. Buried C horizon.
S2	Pale brown silty SAND with some laminations and a blocky soil structure. Becomes more silty and has a columnar structure near the fault. Upper limit is generally gradational on the west wall and sharp on the east wall.
Ps2	Pale brown gravelly (mainly at base of unit) SILT.
W3	Gray silty GRAVEL, becomes less gravelly towards the fault zone and becomes more red brown and less gravelly south of a horizontal distance of 9 m. Upper contacts with unit Ps2 and lower contacts with unit F2 are gradational. On the east wall the contacts with overlying unit Ps2 and underlying F2 are gradational and subtle. On the west wall these units can only be clearly distinguished north of a horizontal distance of 10 m, to the south there is only a subtle and vertically streaked color change – pale brown at the top and the bottom with a band of red brown (W3?).
	Pale brown SILT.
W4a	Brown sandy PEBBLES, not recognized on the west wall.
W4b	Brown silty PEBBLES, not recognized on the west wall.
W4c	Brown cobbly SILT/ silty COBBLES with some sand. There is less coarse materials south of a horizontal distance of 9 m. South of a horizontal distance of 10 m on the east wall, the unit becomes red brown pebbly clayey SILT. South of a horizontal distance of 10 m on the west wall and a horizontal distance of 12 m on the east wall this unit is indistinguishable from the underlying unit F3a and is described as F3b.
F3a	Brown silty PEBBLES grading horizontally to SILT with some pebbles.
F3b	Brown clayey silty PEBBLES with some cobbles.
F3/4u	This unit is used to describe an area of strata where we could not recognize continuous units. Generally there is some colour variation between pale brown and red brown but it is vertically streaked in “flame like” structures which we attribute to dense plant roots probably associated with a phase of wetland vegetation e.g. reeds.
W5a	Brown pebbly silty COBBLES, not recognized on the west wall.
W5b	Red brown silty GRAVEL.
F4a	Brown (pale brown grading upwards to red brown at the southern end of the trench) clayey SILT with some gravel, south of a horizontal distance of 9 m this unit is vertically streaked with red brown.
F4b	Greenish gray (pale brown towards base at the southern end of the trench) silty CLAY. The upper contact of this unit with F4a and the lower contact of unit F4b, with unit F5 is vertically streaked.
S3	Pale brown silty SAND. This unit is mostly very thin and is not present south of a horizontal distance of 9.5 m this unit was not recognized on the east wall.
W6	Brown sandy pebbly silty GRAVEL with some cobbles. Between the horizontal distances of 9 m and 10 m the percentage of coarse clasts decreases from the dominant fraction to nearly absent, therefore unit W6 grades horizontally into unit F5.
F5	Gray brown SILT with some pebbles.
F6a	Pale brown silty CLAY. Grades to the south into unit F6c. Not recognized on the east wall.
F6b	Light pale brown silty CLAY with some sand. Grades to the south into unit F6c. Not recognized on the east wall.
F6c	Red brown near the top of the unit grading down to pale brown clayey SILT, abundant vertical color streaking.
S4	Gray brown fine-medium SAND.
W7a	Gray brown sandy PEBBLES/ Pebbly SAND.

Table A.A-3. (continues on following page).

W7b	Gray Brown Sandy PEBBLES/Pebbly SAND.
F7	Red brown CLAY, grading down into pale brown SILT, grading down into pale brown sandy SILT with some cobbles distributed along the base of the unit.
S5	Gray brown fine-medium SAND.
F8	Brown and gray brown CLAY.
Ga/F8	Gradational transition between units Ga and F8.
S6	Gray brown fine SAND, this unit is seldom thicker than 5 mm. Not exposed on the west wall.
F9	Brown and gray brown CLAY. Not exposed on the west wall.
Ga/F9	Gradational transition between units Ga and F9. Not exposed on the west wall.
Ga	Brown silty GRAVEL and gravelly SILT (varies chaotically) with increased cobble content along the top of this unit.
<b>North of the southernmost fault</b>	
UG	Undifferentiated gravel – Brown silty GRAVEL/ Gravelly SILT. Structure, including package boundaries, destroyed by burrowing animals and to a lesser degree vegetation. Equivalent to units G1-13, which are generally hard to trace.
G1	Gray silty GRAVEL.
G2	Undifferentiated G1 and G3.
G3	Gray brown gravelly silty PEBBLES.
G4	Gray brown PEBBLES clast supported (no matrix) with some cobbles in the southern half of the unit.
G5	Undifferentiated G4 and G6.
G6	Gray brown PEBBLES clast supported with some silt matrix.
G7	Brown silty GRAVEL clast supported.
G8	Undifferentiated G7 and G9.
G9	Brown silty gravelly COBBLES clast supported
G10	Gray brown silty pebbly GRAVEL
G11	Brown silty GRAVEL
G12	Gray brown (gray mottled brown in some places) silty sandy GRAVEL. Not present on the east wall.
G13	Brown silty PEBBLES, horizontally imbricated. This is interpreted as an fissure-infill deposit. Not present on the east wall.
Rg1	Alluviated river gravel (see the unit description for Rg). Gray brown (gray mottled brown in some places) silty sandy GRAVEL.
Rg	River gravel, gray sandy GRAVEL, weakly defined bedding strongly deformed (generally tilting down to the south), many clasts have carbonate coatings on their bottom half, near faults clasts are aligned (near vertical) with their coatings also rotated. We correlate this unit to "Pliocene continental clastics (Cobanlı group)" which form the scarp to the north of the trench [Koçyiğit 1990, p. 157].

**Table A.A-3.** Paleoseismic trench T3: trench log stratigraphic unit descriptions. Symbols used on Figures 7 and 8.

**ANNEX B. Detailed radiocarbon dating information****Bulk sample processing**

A 60-g sub-sample was selected from the bulk sample. The samples were split into two 30 g samples and the following procedures were applied. Samples were submerged in hydrochloric acid (40% HCl) for 24 h, to remove carbonates. Then the samples were placed in hydrofluoric acid (40% HF) for 12 h and continuously agitated, and then they were left in stronger hydrofluoric acid (70% HF) for 7 days, to remove silicates. The samples were then treated with potassium hydroxide (10% KOH) for 15 min, and with hot hydrochloric acid (10% HCl) for 5 min, to remove humic acid as well as additional unwanted organic and inorganic residues. The samples were then sieved and the 10-63  $\mu\text{m}$  fractions of the samples were treated with hot hydrochloric acid (10% HCl) for 5 min. They were then washed and dried, and the samples were recombined (i.e. the two portions of the sample) and submitted to the radiocarbon dating laboratory, where no further chemical pretreatments were administered.

*On the following two pages:*

**Table A.B-1.** Radiocarbon dating data from paleoseismic investigations at Günealan. See text and Figures for description of the event horizons. 'Lab-number' is the unique identifier for each radiocarbon analysis performed by Aeon. In the 'Material' column 'C' stands for charcoal and 'B' stands for bulk sample. 'Yield' is the percentage of carbon in the subsample analyzed. 'Mass' is the mass of the carbon subjected to AMS measurement and does not include the portion used for stable isotope measurement. 'd13C' is the difference between the  $^{13}\text{C}/^{12}\text{C}$  ratio of the sample and that of the VPDB standard, expressed as ‰; values in brackets are estimated. 'FMC' is the  $^{14}\text{C}$  activity ratio, which is corrected for isotopic fractionation and background activity. 'CRA' is the conventional radiocarbon age, normalized to -25 based on a 5568-year half-life. All ages are given at the maximum (Max) or minimum (Min) of the  $2\sigma$  age range.

Trench	Event Horizon	Sample #	Soil unit	Trench wall	Lab Number (Acorn)	Material	Yield (%)	Mass (mg) (3 d.p.)	d13C (vpdp) (3d.p.)	FMC (4.d.p.)	FMC uncertainty	Unrounded CRA (yrsBP) (2.d.p.)		Rounded CRA (yrsBP)		Calibrated age	Order constrained calibrated age
												±	±	±	±		
Trench 1	T1E1	37	C4	E	139	C	49.2	1.198	-26.360	0.9671	0.0041	268.55	33.57	270	35	A.D. 1494–1951	not modeled
	T2E0 and T2E1	42	Ps1a	W	215	C	51.8	1.184	-27.579	0.9801	0.0041	161.70	33.73	160	35	A.D. 1663–1953	not modeled
Trench 2		41	Ps1a	W	141	C	56.9	1.034	-24.485	0.9790	0.0039	170.39	32.11	170	35	A.D. 1657–1953	not modeled
		40	Ps1b	W	140	C	28.6	1.289	-27.896	0.0193	0.0003	31723.31	109.12	31700	150	29995–29559 B.C.	not modeled
		47	Ps1b	E	217	C	3.3	1.286	-27.871	0.8434	0.0033	1367.94	31.44	1370	40	A.D. 608–761	not modeled
		50	S9	E	218	C	59.6	1.304	-27.205	0.9586	0.0040	339.23	33.50	340	35	A.D. 1468–1641	not modeled
Trench 2	T2E2	43	Ps2	W	216	C	59.7	1.257	-26.490	0.8044	0.0049	1748.66	49.02	1750	50	A.D. 137–402	not modeled
		49	Ps3	W	142	C	44.3	1.099	-24.395	0.8069	0.0033	1723.06	32.69	1720	40	A.D. 242–399	not modeled
		26	W2	W	134	C	5.3	1.055	-22.295	0.9158	0.0040	706.84	35.04	710	40	A.D. 1227–1388	reworked
Trench 3	T3E0	2	F1	E	130	C	57.2	1.138	-23.322	0.9930	0.0040	56.58	32.34	60	35	A.D. 1693–modern	A.D. 1706–1926
		B51	Ps2	E	266	B	26.6	1.109	-26.466	0.9816	0.0047	149.38	38.42	150	40	A.D. 1666–1953	A.D. 1666–1888
		B53	F2	E	262	B	36.5	1.102	-24.209	0.9286	0.0036	595.31	31.13	600	35	A.D. 1297–1411	reworked
	T3E1	27	F3b	W	136	C	18.2	1.140	-24.099	0.9338	0.0037	549.92	31.39	550	35	A.D. 1311–1434	A.D. 1337–1440
Trench 3		B54	W4c	E	263	B	25.0	1.319	-24.525	0.9357	0.0038	534.20	32.96	530	35	A.D. 1317–1440	A.D. 1324–1428
		6	W4c	E	132	C	50.6	1.056	-22.888	0.9318	0.0036	567.37	31.36	570	35	A.D. 1304–1425	A.D. 1305–1413
	T3E2	B55	F3a	E	281	B	12.8	1.163	-28.100	0.9069	0.0035	785.03	30.59	790	35	A.D. 1190–1281	A.D. 1189–1280
		5	F3a	E	131	C	28.7	0.648	-25.900	0.9128	0.0035	733.25	31.06	730	35	A.D. 1222–1296	A.D. 1224–1291

B57	F3a	E	282	B	12.0	1.114	-28.700	0.8842	0.0033	988.21	30.35	990	35	A.D. 989–1154	A.D. 989–1153
28	F3/4u	W	227	C	3.2	1.272	-26.176	0.6778	0.0025	3123.95	29.00	3120	30	1490–1314 B.C.	reworked
B60	W5b	E	283	B	6.9	0.867	-27.900	0.8391	0.0038	1409.51	35.84	1410	40	A.D. 576–667	A.D. 578–669
T3E3															
B61	F4a	E	284	B	11.6	1.032	-29.300	0.8027	0.0039	1765.76	39.00	1770	40	A.D. 136–381	A.D. 133–379
B64	F4b	E	285	B	7.0	1.185	-29.500	0.7458	0.0030	2356.06	32.05	2360	40	536–380 B.C.	reworked
25	F4b	W	226	C	2.3	0.808	-26.841	0.6207	0.0026	3830.38	33.80	3830	40	2458–2150 B.C.	reworked
24	F4b	W	225	C	7.0	0.672	-27.627	0.7662	0.0029	2139.63	30.27	2140	40	353–55 B.C.	338–52 B.C.
23	F5	W	224	C	10.0	0.699	(-25)	0.7653	0.0041	2148.84	43.23	2150	50	359–54 B.C.	363–122 B.C.
B68	F5	E	287	B	11.3	0.984	-29.500	0.7238	0.0026	2596.71	28.34	2600	30	815–672 B.C.	811–568 B.C.
33	W6	W	137	C	33.5	1.248	-25.119	0.7892	0.0029	1901.40	29.09	1900	30	A.D. 27–213	too young
T3E4															
12	F6c	E	220	C	4.0	1.064	-28.047	0.5882	0.0021	4262.80	27.99	4260	30	2919–2779 B.C.	reworked
16	F6c	W	221	C	23.1	1.351	-27.085	0.7975	0.0035	1817.79	35.59	1820	40	A.D. 86–323	too young
B70	F6c	E	264	B	26.6	1.330	-24.450	0.7203	0.0028	2635.86	31.49	2640	40	890–774 B.C.	897–789 B.C.
10	F6c	E	236	C	2.4	1.002	-25.729	0.5935	0.0022	4190.86	29.37	4190	30	2889–2676 B.C.	reworked
B71	F6c	E	261	B	17.9	1.115	-24.186	0.6854	0.0023	3033.88	27.11	3030	30	1394–1213 B.C.	1359–1134 B.C.
17	F6c	W	222	C	9.6	0.981	-26.671	0.6870	0.0032	3015.41	37.18	3020	40	1390–1130 B.C.	1347–1127 B.C.
34	F6b	W	138	C	22.7	1.154	-22.9292	0.8120	0.0031	1672.71	30.98	1670	40	A.D. 258–429	too young
B72	S4	E	267	B	3.9	0.401	(-25)	0.6829	0.0029	3064.06	33.86	3060	40	1417–1220 B.C.	1381–1266 B.C.
T3E5															
B73	F7	E	265	B	15.0	1.083	-23.746	0.6640	0.0022	3289.49	26.95	3290	30	1628–1500 B.C.	reworked
9	F8	E	133	C	48.3	0.628	-31.200	0.8193	0.0039	1601.24	37.81	1600	40	A.D. 385–553	too young
B81	F9	E	286	B	37.7	0.887	-29.200	0.6822	0.0023	3071.52	27.22	3070	30	1413–1268 B.C.	1420–1321 B.C.

Trench 3

**Table A.B-1.** Radiocarbon dating data from paleoseismic investigations at Günealan. See text and Figures for description of the event horizons. 'Lab-number' is the unique identifier for each radiocarbon analysis performed by Aeon. In the 'Material' column 'C' stands for charcoal and 'B' stands for bulk sample. 'Yield' is the percentage of carbon in the subsample analyzed. 'Mass' is the mass of the carbon subjected to AMS measurement and does not include the portion used for stable isotope measurement. 'δ13C' is the difference between the <sup>13</sup>C/<sup>12</sup>C ratio of the sample and that of the VPDB standard, expressed as ‰; values in brackets are estimated. 'FMC' is the <sup>14</sup>C activity ratio, which is corrected for isotopic fractionation and background activity. 'CRA' is the conventional radiocarbon age, normalized to -25 based on a 5568-year half-life. All ages are given at the maximum (Max) or minimum (Min) of the 2σ age range.